HHS Public Access

Author manuscript

Cell Metab. Author manuscript; available in PMC 2023 September 06.

Published in final edited form as:

Cell Metab. 2022 September 06; 34(9): 1359–1376.e7. doi:10.1016/j.cmet.2022.07.010.

Neuregulin 4 suppresses NASH-HCC development by restraining tumor-prone liver microenvironment

Peng Zhang[#,1], **Zhimin Chen**[#,1], **Henry Kuang**[#,1], **Tongyu Liu**[1], **Jiaqiang Zhu**[2], **Linkang Zhou**[1], **Qiuyu Wang**[1], **Xuelian Xiong**[1], **Ziyi Meng**[1], **Xiaoxue Qiu**[1], **Ramiah Jacks**[4], **Lu Liu**[3], **Siming Li**[1], **Carey N. Lumeng**[4], **Qing Li**[3], **Xiang Zhou**[2,5], **Jiandie D. Lin**[1,*]

[1]Life Sciences Institute and Department of Cell & Developmental Biology, University of Michigan Medical Center, Ann Arbor, MI 48109

[2]Department of Biostatistics, University of Michigan, Ann Arbor, MI 48109

[3]Department of Internal Medicine and Department of Cell & Developmental Biology, University of Michigan Medical Center, Ann Arbor, MI 48109

[4]Department of Pediatrics and Communicable Diseases, University of Michigan Medical Center, Ann Arbor, MI 48109

[5]Center for Statistical Genetics, University of Michigan, Ann Arbor, MI 48109

Abstract

The mammalian liver comprises heterogeneous cell types within its tissue microenvironment that undergo pathophysiological reprogramming in disease states, such as nonalcoholic steatohepatitis (NASH). Patients with NASH are at increased risk for the development of hepatocellular

[*]Corresponding Author and Lead Contact: Jiandie Lin, Ph.D., 5437 Life Sciences Institute, University of Michigan, 210 Washtenaw Avenue, Ann Arbor, MI 48109, jdlin@umich.edu, Office: (734) 615-3512.

[#]Equal contribution

Author contributions

J.D.L., P.Z. and Z.C. conceived the project and designed research. P.Z., Z.C. H.K., X.X., Z.M., L.Z., X.P. and Q.W. performed the experiments and analyzed the data. T.L., J.Z., S.L., X.Z., X.Q., and J.D.L. performed sequencing data analyses. L.L. and Q.L. contributed to the bone marrow transplantation studies. R.J. and C.N.L. contributed to the macrophage and T cell studies. J.D.L., Z.C., P.Z., T.L. and J.Z. wrote the manuscript.

Online content

Detailed methods, seven supplemental figures (Figure S1-S7) and five supplemental tables (Table S1-S5) are available online.

Competing interests

The authors declare no competing interests.

DATA AND CODE AVAILABILITY

- All RNAseq datasets generated in this work have been deposited into the Gene Expression Omnibus (GEO) database (GSE185042). Raw western blot images can be found at Mendeley link (https://data.mendeley.com/datasets/pgv7xywj5z/1). The raw data supporting the conclusions of this manuscript can be found in Data S1 - Source Data. Original scan of western blots can be found in Figure S8.
- This paper does not report original code.
- Any additional information required to reanalyze the data reported in this paper is available from the lead contact upon request.

carcinoma (HCC). However, the molecular and cellular nature of liver microenvironment remodeling that links NASH to liver carcinogenesis remains obscure. Here we show that diet-induced NASH is characterized by induction of tumor-associated macrophage (TAM)-like macrophages and exhaustion of cytotoxic CD8+ T cells in the liver. The adipocyte-derived endocrine factor Neuregulin 4 (NRG4) serves as a hormonal checkpoint that restrains this pathological reprogramming during NASH. NRG4 deficiency exacerbated the induction of tumor-prone liver immune microenvironment and NASH-related HCC, whereas transgenic NRG4 overexpression elicited protective effects in mice. In a therapeutic setting, recombinant NRG4-Fc fusion protein exhibited remarkable potency in suppressing HCC and prolonged survival in treated mice. These findings pave the way for therapeutic intervention of liver cancer by targeting the NRG4 hormonal checkpoint.

Graphical Abstract

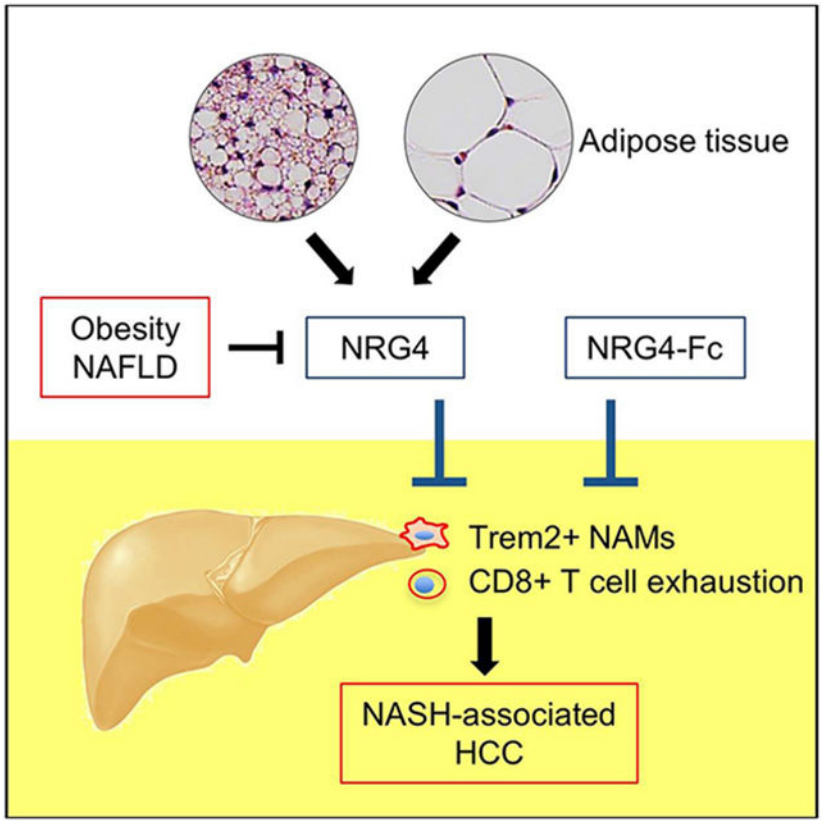

eTOC Blurb

This work illustrates an adipose-hepatic hormonal axis that shapes the liver immune microenvironment. The adipose tissue hormone NRG4 serves as a hormonal checkpoint that restrains the tumor-prone liver microenvironment and suppresses NASH-HCC development. Recombinant NRG4-Fc fusion protein elicits potent therapeutic efficacy against NASH-HCC.

Introduction

The global epidemic of metabolic syndrome markedly increases the prevalence of non-alcoholic fatty liver disease (NAFLD), which is featured by chronic excess fat accumulation in the liver. Several pathogenic mechanisms have been implicated in the development of hepatic steatosis, including insulin resistance, adipose tissue dysfunction, and dysregulations of hepatic lipid metabolism (Cohen et al., 2011; Friedman et al., 2018; Loomba et al., 2021; Rui and Lin, 2022). Hepatic steatosis often exists in a clinically benign state, but frequently progresses to non-alcoholic steatohepatitis (NASH), a more severe metabolic liver disease characterized by persistent liver injury, inflammation, and fibrosis (Ludwig et al., 1980; Sheka et al., 2020; Suzuki and Diehl, 2017). Chronic liver injury in NASH markedly increases the risk for end-stage liver disease such as cirrhosis and liver cancer. Potential therapies targeting diverse pathways, including hepatic metabolism, inflammation, and liver fibrosis, are being evaluated in clinical trials (Friedman et al., 2018). Despite this, no effective pharmacological therapies targeting NASH *per s*e and its associated sequelae are currently available.

The mammalian liver comprises heterogeneous cell types within its tissue microenvironment. The non-parenchymal cells (NPCs) of the liver represent approximately 30% of total liver cells and play an important role in tissue homeostasis, hepatic metabolism, and disease pathogenesis. Recent single-cell RNA sequencing (sc-RNAseq) studies have elucidated the transcriptomic landscape of major liver cell types, including hepatocyte, endothelial cell, hepatic stellate cell (HSC), cholangiocyte and various immune cell types (Ben-Moshe and Itzkovitz, 2019; Ramachandran et al., 2020; Xiong et al., 2020). Several notable themes have emerged from these studies. Beyond cell type differences, striking spatial heterogeneity and differences in cell states have been observed for hepatocytes (Aizarani et al., 2019; Halpern et al., 2017), endothelial cells (Halpern et al., 2018), HSC (Dobie et al., 2019; Rosenthal et al., 2021), and macrophages (Krenkel et al., 2020; MacParland et al., 2018; Ramachandran et al., 2019; Seidman et al., 2020; Xiong et al., 2019a). Secretome gene analysis revealed pervasive intercellular crosstalk via ligand-receptor signaling among different liver cell types and through endocrine mechanisms (Xiong et al., 2019a). An important feature of liver NPCs is that they undergo cell type-specific transcriptomic reprogramming and acquire unique cellular properties under liver disease conditions such as NASH. For example, diet-induced NASH in mice is associated with the emergence of an activated HSC population and the induction of a unique macrophage subtype characterized by high Trem2 expression (Ramachandran et al., 2019; Xiong et al., 2019a). It is conceivable that NASH-associated reprogramming of the liver microenvironment may serve an adaptive role; however, they may represent maladaptive responses that worsen disease progression and/or lead to additional sequelae.

HCC is the most common liver tumor, and at advanced stages, has extremely poor prognosis (Alexander et al., 2013; Kawada et al., 2009; Marengo et al., 2016; Mohamad et al., 2016). Several etiological risk factors have been identified to promote liver carcinogenesis, including chronic viral hepatitis, long-term alcohol use, and NASH; the latter is becoming increasingly common. HCC is strongly associated with liver cirrhosis and represents heterogeneous cancers with different genetic, molecular, and immunological features. In the

context of liver tumorigenesis, several immune cell types, including TAMs, myeloid-derived suppressor cells, and T cells, have been implicated in orchestrating an immunosuppressive and tumor-promoting microenvironment that facilitates HCC development (Giraud et al., 2021; Shalapour and Karin, 2020; Wan et al., 2015). Accumulation of TAMs and T cells with unique transcriptomic signatures has been identified in human liver cancer and linked to poor survival (Sharma et al., 2020; Zhang et al., 2019; Zheng et al., 2017). These findings provide the basis for HCC immunotherapy, which achieves only limited success to date (Feng et al., 2021; Greten et al., 2019; Sangro et al., 2021). Interestingly, approximately 40-50% of HCC in patients with NASH occur in the absence of liver cirrhosis, suggesting that unique pathophysiological factors may underpin the development of NASH-HCC. It is therefore imperative to define the mechanisms responsible for liver carcinogenesis in the context of NASH and uncover novel targets for therapeutic intervention.

We previously identified NRG4 as an adipose tissue-enriched secreted factor that acts on the liver to preserve metabolic health in mice (Chen et al., 2017; Guo et al., 2017; Wang et al., 2014). NRG4 signaling protects hepatocytes from stress-induced injury and attenuates diet-induced NASH pathogenesis. NRG4 expression is markedly downregulated in adipose tissue in diet-induced and genetic obesity models in mice. Importantly, reduced adipose NRG4 expression and plasma levels have been associated with obesity, insulin resistance, and NAFLD in humans (Dai et al., 2015; Li et al., 2021; Wang et al., 2014; Wang et al., 2019). NRG4 signaling has been implicated in the regulation of macrophage survival and function during intestinal inflammation (Schumacher et al., 2021; Schumacher et al., 2017). These intriguing observations prompted us to investigate whether endocrine signaling by NRG4 impinges on the liver immune microenvironment and tumorigenesis in NASH. In this study, we uncover an unexpected role of NRG4 signaling in restraining tumor-prone liver microenvironment and serving as a hormonal checkpoint for NASH-associated liver cancer. Our work provides a proof-of-concept strategy for therapeutic intervention of liver cancer by targeting the NRG4 hormonal checkpoint.

Results

Induction of liver macrophages reminiscent of tumor-associated macrophages during diet-induced NASH

A common feature of solid tumors across diverse tissues including HCC is the induction of immunosuppressive tissue microenvironment that helps cancer cells evade host immune surveillance (Giraud et al., 2021; Shalapour and Karin, 2020; Wan et al., 2015). In this context, induction of TAMs and exhaustion of cytotoxic CD8+ T cells are two hallmarks of the tumor microenvironment. As such, we postulated that NASH pathogenesis might induce reprogramming of intrahepatic immune cell populations to facilitate the development of NASH-associated HCC. To test this, we investigated the transcriptomic states of macrophages and T cells in healthy and NASH livers by analyzing a liver NPC sc-RNAseq dataset we recently generated (Xiong et al., 2019a). UMAP dimensionality reduction analysis identified 11 clusters, corresponding to major cell types in mammalian liver, including endothelial cell, macrophage, T cell, B cell, dendritic cell, cholangiocyte, hepatocyte, and hepatic stellate cell (Figure S1A).

The macrophage cluster contains a total of 7,526 cells and represents the largest immune cell population among NPCs in the liver. Subcluster analysis revealed five macrophage subtypes exhibiting distinct transcriptional signatures (Mac1-5, Figure 1A). Mac1 represents Kupffer cells, the resident macrophage of the liver, whereas Mac2 and Mac4 correspond to classical and non-classical monocytes that can be distinguished by their expression of Ly6c2 and Cd43 (Figure S1B). Mac3 contains macrophages originated primarily from NASH liver (Figure S1C-D), and accordingly, they were termed NASH-associated macrophages (NAMs). A notable feature of NAMs is that they express a set of unique molecular markers, including Apoe, C1qa, Trem2, and Gpnmb (Figure 1B), which have been demonstrated to be enriched in TAMs in skin, liver, lung, breast, bladder, colon, stomach, pancreas and kidney cancers (Bulla et al., 2016; Molgora et al., 2020; Zhang et al., 2019). To visualize this, we performed virtual flow cytometry on the macrophage cluster by gating for single-cell mRNA expression of Csf1r, a pan-macrophage marker, in combination with NAM markers. Compared to chow control, macrophages exhibiting high expression of Apoe, Trem2, and Tgfbr1 were strongly enriched in the livers from NASH mice (Figure 1C).

To track the dynamic regulation of Trem2-expressing macrophages in NASH, we generated a knockin mouse strain that expresses Cre recombinase fused to the C-terminus of the endogenous Trem2 via the self-cleavage 2A peptide. We crossed Trem2-Cre mice with a Rosa26-tdTomato reporter strain to label the Trem2 macrophage lineage. As expected, we found a small number of tdTomato-positive macrophages in chow-fed mouse liver (Figure 1D). Following diet-induced NASH, the abundance of tdTomato-positive cells was markedly increased, some of which formed aggregates that resemble crown-like structure observed in adipose tissue during obesity. We next assessed whether Trem2-positive macrophages are induced during HCC development by combining carcinogen treatment and NASH induction. We treated postnatal day 15 pups with diethylnitrosamine (DEN) and subjected treated mice to NASH diet feeding to model the development of NASH-HCC. Analysis of hepatic gene expression indicated that mRNA levels of liver fibrosis genes (Col1a1, Mmp13) and NAM markers (Mmp12, Trem2, Gpnmb) progressively increased during tumor induction (Figure S1E). Consistent with these results, we observed robust induction of tdTomato-positive macrophages in this NASH liver cancer model (Figure 1D).

Regulation of NASH-associated liver macrophages

We next performed RNA velocity analysis to probe the relationship among different macrophage subtypes. This analysis is based on the relative abundance of unspliced pre-mRNA and mature mRNA to infer the trajectory of cell states. As shown in Figure 1E, we observed notable cell state transitions from classical monocytes to NAMs and KC subclusters. These observations are consistent with previous findings that monocytes provide a cellular source for newly formed Kupffer cells during chronic liver injury and inflammation (Molawi and Sieweke, 2015; Tacke and Zimmermann, 2014). To define the cellular origin of NAMs in NASH liver, we performed bone marrow transplantation using donor cells expressing CD45.1, a pan-hematopoietic cell surface marker, into host mice harboring a distinct allele (CD45.2). Following 6 weeks of feeding a choline-deficient amino acid-defined HFD diet (CDA-HFD), a diet that robustly induces NASH pathologies in mice (Matsumoto et al., 2013; Xiong et al., 2019b), we analyzed CD45 isotype expression on

NAMs using flow cytometry. Remarkably, over 95% of NAMs, as marked by CD9 and GPNMB, displayed CD45.1 expression (Figure 1F), indicating that bone marrow-derived monocytes serve as the primary source of intrahepatic NAMs during NASH.

The emergence of Trem2+ macrophages has been observed in diverse disease states, including Alzheimer's disease, cancer, obesity, NASH, and COVID-19 (Jaitin et al., 2019; Katzenelenbogen et al., 2020; Pilotto et al., 2020; Ulland et al., 2017). However, the nature of the extracellular signals that trigger the induction of this macrophage subpopulation remains largely unknown. To address this, we performed differential gene expression analysis for secreted factors and membrane proteins among five macrophage subclusters. This analysis identified a set of putative ligands exhibiting enriched expression in NAMs, including Pf4, Apoe, Spp1, and Ccl4 (Figure 1G). In addition, we identified a group of 17 genes encoding putative membrane receptors that exhibited preferential expression in NAMs. Several of these genes, including Gpnmb (Zhang et al., 2019), Trem2 (Molgora et al., 2020), Cd74 (Cortes et al., 2017; Klemke et al., 2021), C3ar1 (Magrini et al., 2021), Stab1 (Bostrom et al., 2015), C5ar1 (Medler et al., 2018) have been previously shown to mark TAMs in various cancer types. Violin plots indicate that mRNA expression of Trem2, Tgfbr1, C3ar1, and C5ar1 exhibited higher expression in NAMs compared to other sub clusters (Figure 1H). Interestingly, Mac5, which represents proliferating cells, also displayed elevated expression of these genes, suggesting that macrophages with characteristics of NAMs likely undergo active proliferation in the liver. qPCR analysis revealed that hepatic mRNA expression of all three TGFβ ligands was elevated upon diet-induced NASH in mice (Figure 1I). Analysis of the sc-RNAseq dataset indicated that Tgfb1 is expressed by diverse cell types in the liver, whereas Tgfb2 and Tgfb3 exhibit more restricted expression to cholangiocytes and HSCs (Figure S1F, suggesting that autocrine and paracrine TGFβ signaling may contribute to NAM induction in the liver. To examine whether TGFβ promotes NAM gene expression in a cell-autonomous manner, we performed treatments on bone marrow-derived macrophages (BMDM) and observed that TGFβ robustly stimulated mRNA expression of Trem2, Gpnmb, Apoe, and Tgfbr1 in cultured macrophages (Figure 1J). TGFβ signaling has been implicated in tissue injury response and liver fibrosis in NASH and the induction of immunosuppressive tumor microenvironment (Batlle and Massague, 2019). Our results revealed TGFβ signaling as a common extracellular cue that promotes NAM induction in NASH liver and TAMs during tumorigenesis.

NASH pathogenesis triggers CD8+ T cell exhaustion in the liver

Unlike macrophages, which undergo massive expansion during diet-induced NASH, the total number of T cells remains comparable between chow and NASH groups (Figure S2A). Based on their transcriptomic signature, T cells can be further divided into three subclusters that represent intrahepatic CD8+, CD4+, and Natural Killer T (NKT) cells (Figure 2A). Previous studies have implicated expansion of CD8+ T cells in NASH pathogenesis (Bhattacharjee et al., 2017; Wolf et al., 2014). Differential gene expression analysis on CD8+ subcluster revealed a set of genes dysregulated in NASH (Figure 2B and Table S1). Pathway analysis indicated that the upregulated genes are enriched for chaperone-mediated protein folding, cellular stress response, and TCR and IFNγ signaling, whereas the downregulated genes correspond to cytoplasmic protein translation and lymphocyte

differentiation (Figure S2B). mRNA expression of several genes involved in TCR signaling (Cd3d, Cd3g, Lck) and cytokine response (Ccl3, Ccl4, Ccl5) were increased in CD8+ T cells from NASH mice, likely reflecting persistent stimulation of T cell signaling in the context of liver injury and inflammatory response (Figure 2C). On the contrary, mRNA levels of several T cell stimulatory factors (Icos, Cd40lg, Itgal, Clec4g) were decreased following diet-induced NASH. mRNA expression of many genes involved in protein folding and stress response was elevated in NASH CD8+ T cells, whereas those involved in ribosome biogenesis and mitochondrial oxidative metabolism were suppressed (Figure S2C-D). These results illustrate that intrahepatic CD8+ T cells undergo marked transcriptomic reprogramming following NASH induction.

Among genes upregulated in NASH liver, we noted increased mRNA expression for several genes known to be involved in CD8+ T cell exhaustion, including Pdcd1, Tox, and Eomes (Figure 2C). CD8+ T cell exhaustion has been observed during chronic infection and persistent inflammation and in various cancers (Collier et al., 2021; Wherry and Kurachi, 2015). Impaired effector function and cytokine release by cytotoxic T cells result from excess inhibitory receptor signaling in CD8+ T cells and contribute to defective cancer immunity. Single-cell gene expression analysis revealed that the frequency of CD8+ cells exhibiting high Pdcd1 expression increased from 2.2% to 16.8% (Figure 2D). The frequency of CD8+ T cells with high Tox expression also increased from 9.6% to 27%. In contrast, fewer CD8+ T cells exhibited high expression of Cd40lg and Icos, costimulatory receptors involved in T cell activation. Subcluster analysis of CD8+ T cells revealed four subpopulations that correspond to effector, exhausted, memory, and proliferating T cells (Figure S2E). Exhausted CD8+ T cells were more prevalent in NASH than healthy liver. In contrast, the effector T cell subpopulation was diminished in NASH liver. These results illustrate that CD8+ T cells acquire the molecular characteristics of exhaustion following NASH induction.

Hepatic gene expression analysis indicated that mRNA levels of Pdcd1, Havcr2, Eomes, Lag3, Tigit, and Lilrb4b were strongly increased following diet-induced NASH (Figure 2E). Similarly, mRNA expression of this set of genes was elevated during NASH-HCC development (Figure S1E). We next performed anti-PD1 (encoded by Pdcd1) immunofluorescence staining and flow cytometry to assess T cell exhaustion in NASH liver. While few PD1-positive T cells were observed in the liver from chow-fed mice, they were readily detectable on liver sections from mice subjected to NASH and DEN/NASH treatments (Figure 2F). Flow cytometry analysis indicate that, compared to chow, PD1-high T cells among the CD8+ population was increased from 9.6% to 54.0% in the NASH group (Figure 2G and S2F). Interestingly, CD4+ T cells also showed higher PD1 expression in NASH liver. Consistent with these molecular features of T cell exhaustion, CD8+, but not CD4+, T cells from NASH livers exhibited reduced IFNγ and IL-2 secretion following stimulation with PMA/ionomycin (Figure 2H). Further, proliferation of liver CD8+ T cells in response to CD3/CD28 Dynabeads activation was greatly diminished by NASH, compared to chow control (Figure 2I). To assess the relevance of these findings in human NASH, we performed gene expression analysis on liver biopsies from a cohort of individuals without or with NASH (Guo et al., 2017). As shown in Figure 2J, we found that mRNA

levels of PDCD1, LAG3, EOMES, TIGIT, IKZF2, CD274, and PDCD1LG2 were strongly induced in human NASH livers.

Subclustering analysis of CD4+ T cells identified four subtypes that correspond to Naïve CD4 T cells, regulatory T cells (Tregs), Th17, and Th1 cells (Figure S2G). The abundance of these subtypes in the liver appeared comparable between healthy and NASH mice. Dendritic cells (DCs) play an important role in antigen presentation and adaptive immune response. We uncovered five DC subpopulations based on their marker gene expression: Cd209+, plasmacytoid DC, $Xcr1^{high}$ $Ccr7^{low}$, $Xcr1^{low}$ $Ccr7^{high}$, and dividing DCs (Figure S3A-C). Interestingly, Cd209+ DCs appeared to undergo pronounced expansion in NASH liver (Figure S3D). Taken together, our results illustrate profound reprogramming of the liver immune microenvironment during NASH pathogenesis. The induction of Trem2+ macrophages and exhausted CD8+ T cells may predispose NASH mice to the development of liver cancer.

NRG4 shapes the liver microenvironment and serves as a checkpoint for NASH-associated HCC

We previously identified NRG4 as a fat-derived endocrine factor that regulates hepatic metabolism and NASH pathogenesis (Guo et al., 2017; Wang et al., 2014). Whether NRG4 impinges on the liver immune microenvironment has not been explored. We performed bulk RNA sequencing on liver RNA isolated from NRG4 knockout (KO) mice and wild type (WT) littermate control following six months of NASH diet feeding. Differential gene expression analysis revealed 1,290 and 272 genes exhibiting more than 2-fold changes in mRNA expression (Figure 3A and Table S2). Gene ontology analysis indicate that genes downregulated in NRG4 KO livers were enriched for pathways involved in substrate oxidation, lipid metabolism, and steroid hormone biosynthesis (Figure 3B), whereas upregulated genes were enriched for immune cell adhesion, leukocyte activation, and inflammatory response. Among the upregulated genes are NAM-enriched genes, including Trem2, Gpnmb, Pf4, Ms4a7, Ctsd, Ccr2, Mmp12, H2-Ab1, H2-Aa, and the TGFβ family of ligands (Figure 3C-D). Remarkably, NRG4 deficiency exacerbated NASH-associated induction of genes involved in T cell exhaustion, such as Pdcd1, Tigit, Eomes, and Lag3. In addition, mRNA expression of Cd274, which encodes PD-L1, a PD-1 ligand, and Pdcd1lg2, which encodes PD-L2, also showed increased mRNA expression in the livers from NRG4 KO mice (Figure 3E). These results illustrate that hormonal action of NRG4 exerts a powerful effect on the liver immune microenvironment and raise the possibility that NRG4 may play a role in the development of NASH-associated HCC.

To test this, we induced HCC in NRG4 KO mice and WT littermates using the DEN/NASH protocol (Figure 3F). Under this condition, WT and KO mice gained comparable body weight during the study period (Figure 3G). As expected, we observed tumor nodules of varying sizes in both genotypes (Figure 3H). Compared to control, NRG4 KO mice exhibited signifcantly increased tumor incidents. Total tumor count was 2.6-fold higher in NRG4 KO group than WT control. Both tumors of smaller sizes (<4mm) and larger sizes (>4mm) were increased in the KO group. As a result of increased tumor burden, liver weight to body weight ratio was significantly higher in NRG4 KO group. Blood glucose

levels were slightly lower in the KO cohort, likely due to impairments of hepatic metabolic functions. As such, NRG4 inactivation exacerbates the dysregulations of the liver immune microenvironment and renders mice more prone to development of NASH-associated HCC.

NRG4 restrains tumor-prone liver immune microenvironment during NASH

Having established that NRG4 elicits tumor suppressor activities in the context of NASH-associated liver cancer, we next determined how NRG4 deficiency alters the liver microenvironment at the single-cell level. We performed sc-RNAseq on NPCs isolated from WT and NRG4 KO mouse livers following NASH diet feeding. Similar to previous studies (Xiong et al., 2019a), UMAP analysis revealed a total of 16 clusters that represent eight major liver cell types (endothelial, macrophage, T, B, DC, hepatocyte, cholangiocyte, HSC) expressing unique molecular markers (Figure S4A-C and Table S3). The macrophage cluster contains a total of 12,824 cells and represents the largest population among the NPCs. Subcluster analysis revealed four macrophage subtypes: KC, MDM, NAM, and dividing cells (Figure 4A and S4D). As expected, NAMs displayed prominent expression of Apoe, Trem2, and Gpnmb. While cell counts for the resident macrophage population (KC) remained comparable between two genotypes, we observed a notable expansion of Trem2+ NAMs in NRG4 KO livers, which accounted for approximately 61% of the NAM population (Figure 4B). The MDM and dividing macrophage subclusters also showed expansion in the livers from NRG4 KO mice. Accordingly, immunofluorescence indicated that F4/80, GPNMB, and MHC-II were markedly increased in NRG4 KO livers (Figure 4C). A subset of GPNMB-positive macrophages form “crown-like structures”, similar to those observed in adipose tissue inflammation during obesity. Immunoblotting studies showed that protein levels of TREM2, GPNMB, and MHC-II were elevated in NRG4 KO livers (Figure 4D). These findings demonstrate that NRG4 deficiency promotes the expansion of monocyte-derived Trem2+ macrophages in the liver.

Subcluster analysis of T cells revealed four subtypes: CD4+, CD8+, NKT, and a small group that represents γδT cells (Figure 4E and S5A). Total number of T cells and the CD8+ population showed a notable expansion in NRG4 KO livers. Differential gene expression analysis revealed a group of genes with altered expression in NRG4 KO T cells, as visualized by volcano plot (Figure S5B). The upregulated genes include those involved CD8+ T cell exhaustion, such as Pdcd1, Havcr2, Lag3, and Tox. Interestingly, mRNA expression for genes involved in chaperone-mediated protein folding and stress response (Dnaja1, Hsph1, Hsp90aa1, Hsp90ab1, Hspe1, Hspe8) and chemokine signaling (Ccl3, Ccl4, Ccl5) were also increased. Many down-regulated genes correspond to NKT cell functions, including Xcl1 and members of the Killer cell lectin-like receptor family. Analysis of single-cell gene expression for these markers by virtual flow revealed increased frequency of CD8+ T cells that harbor high levels of expression for Pdcd1 and Lag3 (Figure 4F), indicating that NRG4 deficiency promotes T cell exhaustion in the liver. Pdcd1 and Lag3 double positive CD8+ T cells increased from 12% in WT livers to approximately 42% in NRG4 KO livers (Figure S5C). Together, these results suggest that NRG4 deficiency likely exacerbate pathological reprogramming of T cell transcriptome under metabolic stress conditions.

The exacerbation of T cell exhaustion in mice lacking NRG4 was further confirmed by anti-PD-1 immunofluorescence staining and flow cytometry analysis (Figure 4G-H). As early as three months into NASH diet, PD-1 positive CD8+ T cells increased from 22.1% in WT to 48.2% in NRG4 KO mice. CD8+ T cells isolated from NRG4 KO mouse livers exhibited reduced proliferative response upon activation by CD3/CD28 Dynabeads (Figure 4I). These findings suggest that T cell dysfunction may contribute to increased liver tumorigenesis in NRG4 deficiency. To test this, we performed treatments on WT and NRG4 KO mice subjected to the DEN/NASH tumor protocol with a blocking antibody against PDL1 (anti-PDL1) or IgG2b isotype control (Figure 4J). As recently reported (Wen et al., 2019), anti-PDL1 elicited modest effects on liver tumorigenesis in WT mice. In contrast, PD-L1 blockade significantly reduced tumor counts and maximal tumor size in NRG4 KO livers, suggesting that impaired checkpoint function contributes to increased NASH-HCC incidence in NRG4 KO mice.

Inhibition of tumor-prone liver microenvironment and NASH-HCC by NRG4

We previously demonstrated that adipose Nrg4 expression is markedly reduced in the murine models of dietary and genetic obesity (Chen et al., 2017; Wang et al., 2014). Importantly, lower NRG4 expression is strongly associated with obesity, insulin resistance, and NASH severity in humans (Comas et al., 2019; Jiang et al., 2016; Li et al., 2021; Tutunchi et al., 2020). These observations raise the prospect of restoring NRG4 levels as an effective intervention for the treatment of metabolic disorders. In support of this, transgenic overexpression of NRG4 in adipose tissue results in improved metabolic profiles and protects mice from diet-induced NASH. To assess whether transgenic overexpression of NRG4 restores the liver immune microenvironment and restricts the development of NASH-associated HCC, we subjected cohorts of NRG4 transgenic mice and WT littermates to the DEN/NASH liver cancer protocol, as described above, and analyzed liver tumorigenesis following 20 weeks of NASH diet feeding (Figure 5A). Compared to control, NRG4 TG mice gained slightly less body weight (Figure 5B-C). In contrast to NRG4 deficiency, transgenic overexpression of NRG4 reduced total liver tumor count. While tumors smaller than 4mm were comparable between two groups, the average number of tumors larger than 4mm was significantly reduced in Tg group. Blood glucose levels in the transgenic cohort were higher than control, likely reflecting lower tumor load and improved hepatic function.

Gene expression analysis indicated that mRNA expression of NAM markers (Trem2, Gpnmb) and several other macrophage genes enriched in NAMs (Pf4, Ms4a7, Ccr2, Mmp12) was significantly lower in TG livers (Figure 5D). Likewise, mRNA expression of genes involved in T cell exhaustion was attenuated by transgenic NRG4, including Pdcd1, Lag3, Havcr2, Eomes, and Tigit. Further, markers for activated HSC and liver fibrosis, including Col1a1 and Acta2, also showed reduced expression in the liver from NRG4 TG mice. Together, our data support a crucial role of NRG4 in modulating the liver immune microenvironment and development of NASH-associated HCC.

While immune checkpoint inhibitors have been remarkably successful in treating a wide range of solid tumors, their efficacy in treating HCC remains modest and disappointing (Feng et al., 2021; Greten et al., 2019; Sangro et al., 2021). Because NRG4 appears to

target both macrophages and cytotoxic T cells in the liver, two major aspects of the liver immune microenvironment, we reasoned that this hormonal pathway might provide a unique mechanism of action to elicit therapeutic efficacy against HCC. To test this, we constructed a recombinant adenovirus-associated virus (AAV) vector expressing a secreted fusion protein between amino acids 1-55 of human NRG4 (hNRG4) and the Fc domain of IgG1 (hNRG4-Fc, Figure 5E). These two domains were separated by a glycine-serine (GGGGGS) linker that provides additional spatial flexibility for NRG4 to engage its receptor. To examine whether AAV-mediated overexpression of hNRG4-Fc fusion protein elicits protective effects on NASH, we transduced WT mice fed NASH diet with AAV-Fc or AAV-hNRG4-Fc and continued NASH diet feeding for additional 8 weeks. We detected robust secretion of Fc and hNRG4-Fc fusion protein in plasma from transduced mice (Figure S6A). While hepatic steatosis was comparable between two groups, Sirius red staining and measurements of hydroxyproline content revealed that mice transduced with AAV-hNRG4-Fc exhibited less severe liver fibrosis (Figure 5F-G). Importantly, mRNA expression of NAM-associated genes (Trem2, Gpnmb, Ms4a7, Mmp12) and T cell exhaustion genes (Pdcd1, Havcr2, Lag3, Tigit) was significantly attenuated in response to hNRG4-Fc during NASH progression (Figure 5H).

Suppression of oncogene-induced HCC by recombinant hNRG4-Fc fusion protein

We next generated and affinity-purified recombinant Fc and hNRG4-Fc fusion proteins to evaluate the therapeutic efficacy of NRG4 against NASH-HCC. hNRG4-Fc fusion protein exhibited remarkable stability in circulation with plasma half-life of approximately four days in mice (Figure 6A). hNRG4-Fc elicits stronger ERBB4 phosphorylation compared to untagged NRG4 when tested on Min6 cells expressing the receptor, indicating that the purified fusion protein is biologically active (Figure 6B). We next evaluated the efficacy of hNRG4-Fc in liver tumorigenesis using an oncogene HCC model in combination with NASH feeding in mice. We transduced mice on NASH diet with low doses of recombinant AAV vectors expressing cMYC and activated nRAS oncogenes. We initiated treatments with Fc (2.5 mg/kg) or hNRG4-Fc at two doses (0.5 and 2.5 mg/kg) two weeks following oncogene transduction for four weeks before analysis (Figure 6C). While body weight and plasma metabolite concentrations (glucose, cholesterol, triglycerides) were comparable among three groups following treatments (Figure S6B). Hepatic gene expression analysis indicated that mRNA expression of genes associated with intrahepatic NAM induction and T cell exhaustion was significantly reduced by hNRG4-Fc (Figure 6D).

As expected, we observed numerous tumor nodules in Fc-treated mice (Figure 6E). While low-dose hNRG4-Fc treatment showed a trend to have lower tumor count in treated mice, high-dose hNRG4-Fc elicited a striking reduction of the overall tumor load and maximal tumor size. Total tumor count was decreased by 86.1% in response to 2.5 mg/kg hNRG4-Fc, with small (<4mm) tumors showing a reduction of 84.6%. Further, tumors larger than 4mm were completely absent in mice treated with 2.5 mg/kg hNRG4-Fc. Histological analysis indicated that high-dose hNRG4-Fc treatment resulted in a notable improvement in liver appearance and histology (Figure 6E). Suppression of liver tumorigenesis by hNRG4-Fc resulted in an approximately 60.7% increase in median survival in a separate cohort of mice

(Figure 6F). These results illustrate a potent suppressive effect of hNRG4-Fc fusion protein on HCC development in the context of NASH.

Role of liver immune microenvironment in mediating the therapeutic efficacy of NRG4-Fc in NASH/HCC

We next explored the nature of crosstalk between NRG4 and liver immune microenvironment in mediating its tumor-suppressive effects. RNAseq analysis of total liver RNA isolated from mice treated with Fc or hNRG4-Fc revealed a cluster of differentially regulated genes in response to hNRG4-Fc treatment (Table S4). Pathway analysis indicated that genes downregulated by hNRG4-Fc were enriched for innate immune response, cytokine signaling, and cell adhesion, while upregulated genes were enriched for carboxylic acid, lipid, and steroid metabolism. As expected, mRNA expression of NAM and T cell exhaustion markers were reduced by hNRG4-Fc. To deconvolute cell-type transcriptomic changes, we first identified a total of 1,264 genes that represent cell type markers. Integration of this gene set with the bulk RNAseq data revealed that many genes downregulated by hNRG4-Fc exhibited enriched expression in KC, MDM, and HSC, while hepatocyte genes were enriched in the upregulated gene list (Figure 7A).

To assess whether hNRG4-Fc suppresses NASH/HCC in a cooperative manner with checkpoint inhibitors, we performed treatment studies with hNRG4-Fc and anti-PDL1 alone or in combination. Compared to control, NRG4-Fc elicited a strong tumor-suppressive effects and greatly reduced tumor counts and maximal tumor size in treated mice (Figure 7B). We did not observe significant anti-tumor effects by anti-PDL1 treatment alone. To our surprise, anti-PDL1 slightly diminished the suppressive effects of hNRG4-Fc on HCC development. Recent studies have demonstrated that Trem2 is an important regulator of tumor-associated macrophages and contributes to the immunosuppressive tumor microenvironment (Bulla et al., 2016; Molgora et al., 2020; Zhang et al., 2019). Trem2 inactivation restrains tumorigenesis in mice, in part through augmenting responsiveness to immunotherapy (Molgora et al., 2020). Analysis of The Cancer Genome Atlas (TCGA) liver cancer dataset indicates that hepatic TREM2 expression is a prognostic marker for poor survival (Figure S7B). We next explored whether hNRG4-Fc acts in concert with Trem2 blockade to suppress liver tumorigenesis, we transduced WT and Trem2 KO mice with AAV-cMYC plus AAV-cRAS followed by four weekly treatments with Fc or hNRG4-Fc (Figure 7C). Compared to control, liver tumor burden was significantly reduced in Trem2 KO mice and in WT mice treated with hNRG4-Fc. Remarkably, hNRG4-Fc further augments the tumor-suppressive effects of Trem2 ablation, raising the prospect of achieving enhanced therapeutic efficacy by simultaneously targeting these two pathways.

To explore potential crosstalk between macrophages and CD8+ T cells, we performed ligand receptor pairing analysis using CellPhoneDB, a tool developed for prediction of intercellular signaling using sc-RNAseq data (Efremova et al., 2020). Our analysis revealed a network of reciprocal ligand and receptor signaling between these two cell types (Figure S7A). Importantly, the landscape of predicted ligand and receptor interaction was profoundly altered upon NASH induction. Notably, inhibitory receptor signaling mediated by PD1 appeared to be augmented in CD8+ T cells from NASH livers. To directly test whether

Trem2 plays a role in the regulation of CD8+ T cells, we cultured splenic CD8+ T cells isolated from OT-1 transgenic mice with WT or Trem2 KO BMDMs chased with ovalbumin (OVA) peptide. Interestingly, Trem2 deficient macrophages markedly enhanced CD8+ T cell proliferation in an OVA-independent manner (Figure 7D). At low OVA concentration, we also observed a more robust proliferative response when T cells were exposed to Trem2 KO BMDMs. Together, these findings suggest that Trem2 may exert an inhibitory effect on T cell proliferation during NASH-HCC development.

Discussion

Reprogramming of the liver microenvironment is a core feature of NASH pathogenesis, which encompasses altered hepatic metabolism, activation of tissue injury response, and engagement of various immune cells. The molecular and cellular nature of the altered immune interface and its role in the development of NASH-associated HCC remain obscure. In this study, we performed single-cell transcriptomic analysis and identified two notable features of the liver immune microenvironment during NASH pathogenesis: expansion of macrophages with molecular characteristics of tumor-associated macrophages and induction of CD8+ T cell exhaustion. The adipose endocrine factor NRG4 serves as a hormonal checkpoint that restrains these features of tumor-prone liver microenvironment and suppresses HCC development (Figure 7E).

NASH-associated macrophages are characterized by abundant expression of several molecular markers of TAMs, including Trem2, Gpnmb, Apoe, and C1qa. The emergence of Trem2-expressing macrophages has also been detected in cirrhotic livers and other disease conditions in humans (Mulder et al., 2021; Ramachandran et al., 2019), indicating that this is a conserved feature of liver diseases. Consistently, single-cell studies have demonstrated that Trem2-expressing macrophages are increased in several cancers, including liver cancer, and is inversely associated with survival in certain cancer types (Molgora et al., 2020; Mulder et al., 2021; Obradovic et al., 2021). In the context of tumorigenesis, Trem2 appears to exert tumor-promoting activities, in part through modulating T cell function (Molgora et al., 2020). The striking similarity between NAMs and TAMs raises the possibility that NAM induction during NASH may contribute to the formation of tumor-promoting microenvironment in the liver. In parallel, CD8+ T cells acquire a transcriptomic signature characteristic of T cell exhaustion. The latter is commonly observed during chronic infection and cancer (McLane et al., 2019). In the context of NASH pathogenesis, it is likely that persistent liver injury resulting from metabolic stress triggers prolonged activation of adaptive T cell response, ultimately leading to impaired cytotoxic T cell function. Induction of T cell exhaustion may serve a protective mechanism to limit further liver injury caused by cytotoxic T cell function (Dudek et al., 2021; Pfister et al., 2021). In this case, checkpoint inhibitor treatments worsen liver injury in diet-induced NASH mice, thereby limiting immunotherapy targeting HCC. It is notable that induction of NAMs and T cell exhaustion during diet-induced NASH occurs before any noticeable tumors develop in the liver, raising the possibility that these immune dysregulations promote an immunosuppressive liver microenvironment prone to liver carcinogenesis.

Inter-organ crosstalk via endocrine hormones is fundamental to the maintenance of metabolic homeostasis in mammals. NRG4 is a fat-derived secreted factor that mediates adipose-hepatic crosstalk and ameliorates diet-induced NASH pathogenesis in mice (Dudek et al., 2021; Pfister et al., 2021). Several lines of evidence support a newly uncovered role of NRG4 in the regulation of liver immune microenvironment and the development of NASH-associated HCC. First, NRG4 deficiency augments NAM induction and exacerbates intrahepatic CD8+ T cell exhaustion following diet-induced NASH in mice, as revealed by bulk RNA sequencing and single-cell transcriptomic studies. On the contrary, elevating NRG4 levels by transgenic or AAV-mediated overexpression suppresses the induction of NAM markers and genes associated with T cell exhaustion. Given the striking resemblance of the transcriptomic landscape of NASH macrophages and T cells and those in the tumor microenvironment, our findings suggest that NRG4 may function as a hormonal checkpoint to restrain the tumor-prone immune characteristics. In support of this, NRG4 transgenic mice had alleviated, whereas the null mice exhibited more severe DEN-induced tumor burden in the context of NASH. Importantly, PDL1 blockade ameliorated NASH-HCC in NRG4 KO mice, underscoring an important role of T cell dysfunction in mediating the effects of NRG4 deficiency on liver cancer. In a therapeutic setting, NRG4-Fc fusion protein elicited remarkable protection against HCC development and prolonged survival. While hNRG4-Fc did not elicit significant synergy with PDL1 blockade, we observed an additive effect of the fusion protein and Trem2 deficiency in restricting liver tumor development. These findings illustrate a potential therapeutic window for treating NASH-associated HCC using NRG4-based biologics alone or in combination with Trem2 blockade.

The exact molecular signaling mechanisms that mediate the effects of NRG4 on NAM induction and T cell exhaustion remain currently unknown. It is possible that NRG4 may directly act on these immune cell types to regulate their gene expression and functions. Previous studies have demonstrated that ErbB4, the cellular receptor for NRG4, is present on macrophages and mediates the effects of NRG4 on macrophage survival and function (Schumacher et al., 2021; Schumacher et al., 2017). However, ErbB4 expression is low on intrahepatic macrophages and T cells, based on sc-RNAseq analysis. As such, it is likely that NRG4 exerts its effects on the immune cell types in the liver via indirect mechanisms. Within the liver, ErbB4 expression is observed in hepatocytes and cholangiocytes. Interestingly, liver-specific ErbB4 knockout mice are more prone to liver injury and DEN-induced HCC (Liu et al., 2017). ERBB4 expression is frequently reduced in cancers and cancer cell lines (Segers et al., 2020), supporting a potential tumor suppressor role of NRG4-ERBB4 signaling. Whether NRG4 modulates the release of paracrine signals from hepatocytes and cholangiocytes to influence NAM induction and T cell exhaustion during diet-induced NASH warrants additional future investigation. The ability of NRG4 to exert effects on multiple aspects of liver biology, including hepatic lipid metabolism, hepatocyte injury, and the immune microenvironment, strongly suggests that this hormonal pathway may provide an attractive target for therapeutic intervention of NASH-associated HCC. Multiple immunotherapy strategies are currently under evaluation for the treatment of HCC with mixed success (Giraud et al., 2021; Greten et al., 2019). It is therefore tempting to envision that NRG4 fusion protein may act in synergy with kinase inhibitors and/or checkpoint inhibitors to elicit more robust therapeutic efficacy.

Limitations of study

The current study has several limitations that warrant future investigation. Liver cancers induced by chemical carcinogen and oncogene overexpression in combination with NASH diet feeding may not fully recapitulate the pathophysiological features of liver carcinogenesis in patients with NASH. While human NRG4-Fc fusion protein was used in this study, whether it exhibits efficacy in shaping human liver immune microenvironment and HCC progression remains to be evaluated. Our study does not address how NRG4 impacts on intratumor immune microenvironment, which may contribute to its anti-tumor effects. Finally, the exact cellular and molecular nature of NRG4 signaling that mediate its tumor-suppressor function remains an important unanswered question. Clarifying this aspect of NRG4 action will likely further improve NRG4-based therapeutic strategies.

STAR★Methods

RESOURCE AVAILABILITY

Lead contact—Jiandie Lin (jdlin@umich.edu).

Materials Availability—Further information and request for materials should be directed to and will be fulfilled by the lead contact.

EXPERIMENTAL MODEL AND SUBJECT DETAILS

Human study—Normal or NASH human liver tissues were obtained from the Liver Tissue Cell Distribution System at the University of Minnesota (Minneapolis, Minnesota, USA) (Guo et al., 2017). Both male and female individuals were included. The average ages for normal individuals and NASH patients were 55.8 and 52.5 years old, respectively. Individuals with an alcohol-drinking history (2 to 3 drinks/day) and liver cancer were excluded from the study.

Animal studies—All animal studies were performed following procedures approved by the Institutional Animal Care & Use Committee at the University of Michigan. Mice were housed in pathogen-free facilities under 12-h light-dark cycles with free access to food (Teklad 5001 Laboratory Diet) and water. Nrg4 KO mice were generated at the University of Michigan Transgenic Animal Model Core using Nrg4 $^{tm1a(EUCOMM)Hmgu}$ ES cells purchased from the International Mouse Phenotyping Consortium. Whole body Nrg4 KO mice were generated by crossing Nrg4 flox mice with Ella-Cre mice (a gift from Dr. David Ginsburg, University of Michigan). Trem2 KO mice were purchased from The Jackson Laboratory (Strain #027197). OT-I transgenic mice and Rosa26-tdTomato reporter mice were kindly provided by Dr. Weiping Zou and Dr. Jun Wu (University of Michigan), respectively. We generated Trem2-Cre knockin mouse strain that contains Cre recombinase fused to endogenous Trem2 via the self-cleavage P2A peptide. Trem2-Cre mice were crossed with the Rosa26-tdTomato reporter strain to label the Trem2-expressing macrophage lineage. Generation of adipose-specific Nrg4 transgenic mice was described previously (Wang et al., 2014).

We did not predetermine sample sizes; instead, we selected group sizes based on contemporary work in the literature. We randomly assigned mice of the same genotype to different treatments to minimize any potential bias. The investigators were not blinded to allocation during experiments and outcome assessment. We excluded mice that exhibited skin lesions due to fighting and growth retardation due to malocclusion.

METHOD DETAILS

NPC isolation, BMDM culture and cell lines—For hepatic macrophages, liver samples were filtered through 100 μm strainers in 1% FBS, 1mM EDTA in PBS and centrifuged at 50 g for 3 minutes to remove hepatocytes. For hepatic T cells, liver tissues were minced briefly and immersed in 3 mL of RPMI 1640 plus 2 mg/mL collagenase IV and 0.1 mg/mL DNase I at 37 °C for 20 minutes with periodic agitation. Liver tissue was then filtered through a 100μm strainer and spun at 50 g for 3 minutes to remove hepatocytes. NPCs were harvested as intermediate fraction following gradient centrifugation in 25% optiprep at 1,500 g for 20 minutes. Cells were then treated with 0.8% NH4Cl for 5 minutes to lyse red blood cells. CD8+ T cells were enriched with negative selection kit (Miltenyi, 130-096-495) following manufacturer's instruction.

BMDM were differentiated from bone marrow cells harvested from the epiphyses of tibia and femur bones from 6- to 8-week-old mice. Bone marrow cell suspension was filtered through a 70 μm cell strainer, centrifuged at 250g for 5 minutes. Cells pellets were resuspended in DMEM and treated with 0.8% NH_4Cl for 5 minutes to lyse red blood cells. BMDM was cultured in DMEM supplemented with 10% bovine growth serum, 100 μg /mL penicillin, 100 μg/mL streptomycin, and 25 ng/mL M-CSF (BioLegend). Following seven days of culture, BMDMs were treated with vehicle or 2.5ng/mL TGFβ for 24 hrs.

Suspension cell line, Expi293F™, was purchased from Thermo Fisher Scientific and cultured with Expi293™ Expression Medium in Corning spinner flask at 37°C incubator with humidified atmosphere of 8% CO_2. Min6 cells stably expressing ErbB4 were a gift from Dr. Peter Dempsey (University of Michigan), and were cultured in DMEM supplemented with 15% FBS, 1.7g/500mL sodium bicarbonate, 2.5ul/500mL β-mercaptoethanol and 1% Pen/Strep. Before conditioned media treatment (for 15min), the cells were starved in serum-free DMEM for 4 hrs.

NASH models—For diet-induced NASH, mice were fed a diet containing 40 kcal% fat, 20 kcal% fructose, and 2% cholesterol (Amylin diet, D09100310, Research Diets Inc.), as previously described (Guo et al., 2017; Xiong et al., 2019a). In a separate diet-induced NASH model, C57BL/6 mice were maintained on Choline-Deficient, Amino acid-defined HFD (45 kcal% fat) containing 0.1% methionine (CDA-HFD diet, A06071309, Research Diets Inc.) for 6 weeks. (Xiong et al., 2019a).

HCC models, treatment, and analysis—For DEN/NASH HCC model, male pups were injected with a single i.p. dose of DEN (25 mg/kg body weight, Millipore-Sigma) on postpartum day 15. Mice were switched to NASH diet at two months of age and analyzed 5-6 months later. For quantification, HCC tumor numbers and the largest tumor sizes were determined by counting the number of visible tumors and measuring the size of the largest

tumor with a caliper, respectively. Plasma concentrations of ALT, AST and cholesterol were measured using commercial assay kits (Stanbio Laboratory). Plasma concentrations of TAG was measured using Sigma kits.

For oncogene NASH HCC model, male mice were put on NASH diet for two weeks before a single tail vein injection of the AAV-oncogene cocktail (AAV8-cMyc $6X10^9$ genome copies/mouse + AAV8-nRAS-V12 $6X10^9$ genome copies/mouse). Two weeks after tumor induction, mice received weekly treatments of Fc or hNRG4-Fc at a dose of 0.5 or 2.5 mg/kg for four weeks before tumor analysis. For survival experiment, male mice were injected $9X10^9$ genome copies/mouse AAV8-cMyc and $9X10^9$ genome copies/mouse AAV8-nRAS-V12 via tail vein. Two weeks following transduction, mice were treated with Fc or hNRG4-Fc (1.5 mg/kg) weekly through intraperitoneal injection for a total of four weeks and monitored until they reached the tumor study end point. For hNRG4-Fc and anti-PDL1 co-treatment study, C57BL/6 mice were fed NASH diet for two weeks before AAV-oncogene transduction. At week 4, 100 μg isotype control (IgG2b) or anti-PDL1 was administered intraperitoneally to each mouse twice per week; 1.5 mg/kg Fc or hNRG4-Fc was intraperitoneally injected to mice weekly. This treatment schedule lasted four weeks and tumor burden was analyzed two weeks after the treatments. For Trem2 KO mouse study, WT and Trem2 KO mice were injected the AAV-oncogene cocktail after two weeks of NASH diet feeding. Two weeks later, 1.5 mg/kg Fc or hNRG4-Fc was intraperitoneally injected to mice weekly for a total of four weeks. Tumor burden was analyzed two weeks after the end of the treatments.

Bulk RNA sequencing and gene expression analysis—Total RNA was extracted from frozen livers or harvested cells using Trizol (Alkali Scientific, TRZ-100). Bulk liver RNA sequencing was performed by BGI Global Genomic Services. The RNA-seq reads alignment was performed using the STAR aligner (version 2.7.4a) against the mouse genome assembly release mouse_GRCm38.p6 from NCBI and gene annotation release M25 from GENCODE. The mapped reads for each gene were quantified using the featureCounts function from the Rsubread package (version 2.0.1) in the R environment (version 4.0.0). Differences in transcript abundance between different genotypes were calculated for each gene using the R package DESeq2 (version 1.30.0). Genes with adjusted P-value < 0.05 were considered differentially expressed. Quantitative RT-PCR gene expression analysis was performed as previously described (Li et al., 2008). A list of qPCR primers is shown in Table S5.

Isolation and scRNA-seq analysis of liver NPCs—Liver NPCs were isolated following a two-step protocol of pronase/collagenase digestion (Mederacke et al., 2015). Briefly, the liver was perfused *in situ* with calcium-free Hank's Balanced Salt Solution (HBSS) containing 0.2 mg/mL EDTA, followed by sequential perfusion with 0.4mg/mL pronase (Sigma, P5147) and 0.2% collagenase type II (Worthington, LS004196). The liver was minced and further digested with HBSS containing 0.2% collagenase type II, 0.4 mg/mL pronase and 0.1mg/mL DNase I (Roche, R104159001) in 37 °C water bath with shaking for 20 min. Digestion was terminated with DMEM containing 10% serum. The resulting liver cell suspension was centrifuged at 50 g for 3 min to remove hepatocytes and

passed through a 30 μm nylon cell strainer followed by treatment with 0.8% NH_4Cl to lyse red blood cells. This resulting cell suspension was centrifuged, resuspended in HBSS, and subjected to density gradient centrifugation using 20% Optiprep (Axis Shield, 1114542) to remove dead cells. Cell viability was confirmed by trypan blue exclusion. The resulting NPCs were subjected to scRNA-seq analysis using 10X Genomics Chromium Single-Cell 3' at the University of Michigan Advanced Genomics Core, as previously described (Xiong et al., 2019a).

Bone marrow transplantation—Bone marrow cells were acquired from the femurs of donor (45.1) with Hank's buffered salt solution without calcium or magnesium, supplemented with 2% heat-inactivated calf serum (HBSS; Invitrogen). Cells were triturated and filtered through nylon screen (70 μm; Sefar America) to obtain a single-cell suspension. Recipient B6 mice (CD45.2) were irradiated in an Orthovoltage X-ray source delivering 300 rad min^{-1} in two equal doses of 540 rad, delivered 2 h apart. Cells were injected into intravenously through the tail. 6 weeks post-transplant blood was obtained from the tail veins of recipient mice, subject to ammonium-chloride potassium red cell lysis, and stained to monitor engraftment with CD45.2 (104), CD45.1 (A20), Cd11b (M1/80), Gr-1 (8C5).

Flow cytometry—1 x 10^6 liver NPC cells were incubated with 100 μl of various antibodies diluted at optimal concentrations for 40 min at 4 °C. The following fluorochrome-conjugated antibodies were used: CD45.2 (104; Biolegend, 109831), CD45.1 (A20; Biolegend, 110741), CD45 (30-F11; Biolegend, 103126) F4/80 (BM8; Biolegend, 123114), CD11b (M1/70; Biolegend, 101227), CD9 (MZ3; Biolegend, 124805), GPNMB (CSTREVL; Thermo Fisher, 50-5708-82), CD90.2 (30-H12; Biolegend, 105335), CD4 (GK1.5; Biolegend, 100407), CD8 (53-6.7; Biolegend, 100734), PD-1 (29F.1A12; Biolegend, 135218), IL-2 (JES6-5H4; Biolegend, 503807). Liver macrophages were gated as $CD45+F4/80^{hi}CD11b^{int}$ and $CD45+F4/80^{int}CD11b^{hi}$ for KC or MDM, respectively. For intracellular staining, 1 x 10^6 NPCs were cultured in complete RMPI 1640 medium with Brefeldin A and PMA/ionomycin for 6 hours before harvested for flow staining. After surface staining, fixed cells were permeabilized using Invitrogen transcription factor staining buffer set according to manufacturer's protocol. Samples were analyzed using BD LSR cell analyzer at the Vision Research Core Facility at the University of Michigan Medical School or Attune NXT4 Flow Cytometer at MCDB research core facility at the University of Michigan. Data were analyzed using the CellQuest software (BD Biosciences) or Attene NXT software and Flowjo (Flowjo.com).

T cell proliferation assay—Spleen from OT-I mice were crushed through 70 um cell strainers with complete RPMI 1640. Splenocytes were pelleted and then treated with 0.8% NH_4Cl for 5 minutes to lyse red blood cells. CD8+ T cells were enriched using negative selection kit (Miltenyi, 130-096-495) per manufacture's instruction. CD8+ T cells were counted and labeled with CFSE Cell Division Tracker Kit (Biolegend, 423801). Fully differentiated BMDMs were scraped off from culture dish and reseeded into 96 well plate at a density of 1 x 10^5 cell per well. Two hours after seeding, BMDMs were pulsed with $OVA_{257-264}$ peptide at indicated concentrations for 2 hours, washed three times with

RPMI 1640, and incubated with 1 x 10^5 cell labeled OT-I CD8+ T cells for 5 days. Cell proliferation rate was determined by flow cytometry.

For intrahepatic T cell proliferation, NPCs were harvested from liver tissue and labeled with CFSE Cell Division Tracker Kit (Biolegend, 423801). Labeled cells were transferred to 96-well plates and stimulated with CD3/CD28 Dynabeads for up to 5 days. Cell proliferation rate was determined by flow cytometry.

Immunofluorescence staining and tissue histology—Liver tissues were fixed *in situ* with 4% paraformaldehyde, incubated with 30% sucrose in PBS overnight, and embedded in OCT. Frozen sections were permeabilized with 0.3% Triton X-100 in PBS and then blocked in 5% BSA, followed by incubation in primary antibody solution overnight at 4 °C, and subsequently in secondary antibody solution at room temperature for one hour. Sections were mounted in VECTASHIELD Antifade Mounting Medium (Vector Laboratories, H-1000). Images were taken with Leica SP5 Confocal Imaging System and SP8 Lightning Confocal Microscope System.

For histology, formalin-fixed, paraffin-embedded mouse liver sections were stained with H&E to evaluate steatosis and inflammatory cell infiltration. Liver fibrosis was assessed by Picrosirius (sirius) red (Polysciences, catalog 24901) staining of the formalin-fixed, paraffin-embedded mouse liver sections.

Hydroxyproline assay—Collagen content in the livers was evaluated by measuring the hydroxyproline level in the livers using the Hydroxyproline Colorimetric Assay Kit (K555-100) from BioVision. Briefly, liver tissue was homogenized in water and samples were hydrolyzed by incubation with 6N hydrochloric acid at 120°C for 3 hours. Liver hydrolysates were oxidized using chloramine-T, followed by incubation with Ehrlich's perchloric acid reagent for color development. Absorbance was measured at 560 nm, and hydroxyproline quantities were calculated by reference to standards processed in parallel.

Construction, generation, and purification of hNRG4-Fc fusion protein—The NRG4-Fc fusion construct contains an N-terminal signal peptide from azurocidin 1 followed by the EGF-like domain of human NRG4 (amino acids 1-55), a glycine-serine linker and human IgG1 Fc fragment. The construct was synthesized by GeneArt (Thermo Fisher Scientific) and subcloned into pcDNA3 expression vector. For fusion protein production, the Fc vector and NRG4-Fc constructs were transiently transfected into suspension Expi293F™ cells using the Expi293 Expression System (Thermo Fisher Scientific). Media was collected 7 days after transfection, adjusted to the composition of binding buffer (0.2 M sodium phosphate, pH 7.0), filtered through a 0.45-μm filter (Millipore), and processed for affinity purification using a Hitrap rProtein A FF 5 mL column on the ÄKTA Pure FPLC chromatography system (GE Healthcare). The column was washed with 50 mL binding buffer and eluted with a pH 3-7 gradient elution buffer (0.1 M sodium citrate, pH 3.0). Fusion proteins were dialyzed in 1× phosphate-buffered saline buffer (137 mM NaCl, 2.7 mM KCl, 10 mM Na2HPO4, 1.8 mM KH2PO4, pH 7.4) using a Slide-A-Lyzer Dialysis Cassette (Thermo Fisher Scientific). For measurements of hNRG4-Fc plasma half-life, male C57BL/6J mice received an i.p. injection of hNRG4-Fc (2 mg/kg body weight). NRG4-Fc

fusion protein was quantified using an ELISA kit for human IgG1 Fc (Bethyl Laboratories Inc.), as previously described (Zhang et al., 2018).

Sandwich ELISA for hNRG4-Fc measurement—Goat anti-human polyvalent immunoglobulins antibody (Sigma, I1761) was diluted in 100mM sodium carbonate buffer (pH=9.6) at 1:1000 ratio for coating ELISA plates at 4°C overnight. The plates were washed with wash buffer (PBS + 0.5% triton-x100) for three times. After blocking with 5% BSA for 1 hours at room temperature, 100ul of diluted samples or human Fc standard (Thermo Fisher, 10702-HNAH-5) were added to each well and incubated for 2 hours at room temperature. After washing, diluted HRP-conjugated goat anti-human IgG (Fc specific) antibody (Sigma, A0170) in 5% BSA was added to the wells. Color was developed using TMB reagent (Thermo Fisher, PI-34028) after 1 hour following manufacturer's instruction.

Immunoblotting analysis—For total lysates, livers were homogenized in a lysis buffer containing 50 mM Tris (pH 7.5), 150 mM NaCl, 5 mM NaF, 25 mM β-glycerol phosphate, 1 mM sodium orthovanadate, 10% glycerol, 1% Triton X-100, 1 mM dithiothreitol (DTT), and freshly added protease inhibitors (Roche). Cells were harvested and homogenized with lysis buffer containing 2% sodium dodecyl sulfate (SDS), 50 mM Tris-HCl (pH 6.8), 10 mM DTT, 10% glycerol, 0.002% bromphenol blue, and freshly added protease inhibitors. Immunoblotting experiments were performed using specific antibodies. For immunoblots, antibodies phospho-ErbB4 (Y1284) (catalog 4757), total ErbB4 (catalog 4795) were from Cell Signaling Technology. Antibody against Hsp90 (Sc-13119) and tubulin (Sc-32293) were purchased from Santa Cruz. Gpnmb antibody (AF2330) was purchased from R&D. Antibody against Fc (A10648), MHC-II (14-5321-85) were purchased from Invitrogen. Trem2 antibody was a generous gift from Dr. Marco Colonna (Washington University).

QUANTIFICATION AND STATISTICAL ANALYSIS

The statistical details of the experiments are described in figure legends.

Data analysis—Processing of the sc-RNAseq dataset for chow and NASH NPCs (GSE129516) was previously described (Xiong et al., 2019a). For Nrg4 WT and KO NPC scRNA-seq dataset, gene expression matrix for each sc-RNAseq sample was generated by CellRanger. Pipeline (10x Genomics) and raw data were processed further with Seurat package (version 3.1.2) (Stuart et al., 2019). Specifically, genes expressed by less than 3 cells were excluded from further analysis. Cells with fewer than 200 detectable genes, greater than 8,750 genes or greater than 20% mitochondrial genes were exclused from analysis. After removing potential doublets, a final dataset with 19,567 genes measured on 33,044 cells were used for downstream analysis.

For both datasets, filtered gene expression counts for each cell were log-normalized with a scale factor of 10,000. To remove potential batch effects, top 2,000 informative genes were selected for each sample through the variance stabilizing transformation and used for the further data integration through the canonical correlation analysis (CCA).

Clustering and cell typing—After aligning the top 30 dimensions according to CCA, principal component analysis (PCA) was performed on the integrated data and the first

100 PCs were extracted. An elbow algorithm was used to find the optimal number of PCs to construct Uniform Manifold Approximation and Projection (UMAP) plots. Cells were clustered using the unsupervised learning algorithm with a resolution of 0.1. The cluster marker genes were collected using the Wilcoxon rank-sum test between the cells in a single cluster and all other cells with log fold change threshold of 0.25. The identity for each cluster was further assigned based on the prior knowledge of marker genes. Sub-clustering analysis were performed at higher resolutions for the major cell types, including T cells, macrophages, and dendritic cells.

Data visualization—To generate virtual flow, the normalized UMI count matrix was adjusted by adding a normally distributed noise with a mean of 1.0 and standard deviation of 0.1. The plots were generated by ggplot2. The gradient colors were scaled by estimated count. Feature plots, dot plots, violin plots, and heatmaps were generated by Seurat, pheatmap or ggplot2 in R. The differential expressed genes in volcano plots were determined by Wilcoxon rank-sum test between the cells in different genotypes or diet conditions within one cell cluster.

RNA velocity analysis—RNA velocity analysis was performed using the scVelo (0.2.2) implemented in python (La Manno et al., 2018). Bam files were first converted to loom files using the velocyto based on the mm10 annotation files. Cells identified as macrophage (n=7,526) were extracted from the loom files for all samples and used for the velocity analysis. The extracted data were filtered and normalized with default parameters. After the moments (first and second) calculation, the velocities were obtained by modeling the transcriptional dynamics of splicing kinetics stochastically. The UMAP coordinates from the Seurat analysis were used as basis for the visualization.

CellPhoneDB analysis—CellPhoneDB (v3) was used to analyze intercellular communication between CD8+ T cells and macrophages for chow and NASH samples (Efremova et al., 2020). We used version 2.0.0 of the database (1396 interactions) with default parameters (10% of cells expressing the ligand/receptor). A permutation test (10,000 permutations) was applied to determine statistical significance. Interactions with $P < 0.05$ were considered significant. Due to the lack of intercellular interaction database for mice in CellPhoneDB, we generated the mouse ligand-receptor interaction gene list based on human orthologs utilizing the R package biomaRt.

Supplementary Material

Refer to Web version on PubMed Central for supplementary material.

Acknowledgements

We thank Dr. Marco Colonna (Washington University) for sharing anti-Trem2 antibody, Dr. Weiping Zou (University of Michigan) for providing OT-I transgenic mice, Dr. David Olson (University of Michigan) for designing the Trem2-Cre knockin strategy, Dr. Jun Wu (University of Michigan) for providing tdTomato mice, Dr. Xin Chen (UCSF) for sharing the cMYC and nRAS plasmids, and Xiaoling Peng for technical assistance. This work was supported by NIH (DK102456 and DK118731 to J.D.L.) and a pilot grant from the University of Michigan Rogel Cancer Center. H.K. was supported by an NRSA fellowship (FDK117615) and MSTP training grant (T32GM007863). L.Z. was supported by the American Heart Association Career Development Award. T.L. was supported by Patten Predoctoral Fellowship provided by the University of Michigan.

References

Aizarani N, Saviano A, Sagar, Mailly L, Durand S, Herman JS, Pessaux P, Baumert TF, and Grun D (2019). A human liver cell atlas reveals heterogeneity and epithelial progenitors. Nature 572, 199–204. [PubMed: 31292543]

Alexander J, Torbenson M, Wu TT, and Yeh MM (2013). Non-alcoholic fatty liver disease contributes to hepatocarcinogenesis in non-cirrhotic liver: a clinical and pathological study. J Gastroenterol Hepatol 28, 848–854. [PubMed: 23302015]

Batlle E, and Massague J (2019). Transforming Growth Factor-beta Signaling in Immunity and Cancer. Immunity 50, 924–940. [PubMed: 30995507]

Ben-Moshe S, and Itzkovitz S (2019). Spatial heterogeneity in the mammalian liver. Nat Rev Gastroenterol Hepatol 16, 395–410. [PubMed: 30936469]

Bhattacharjee J, Kirby M, Softic S, Miles L, Salazar-Gonzalez RM, Shivakumar P, and Kohli R (2017). Hepatic Natural Killer T-cell and CD8+ T-cell Signatures in Mice with Nonalcoholic Steatohepatitis. Hepatol Commun 1, 299–310. [PubMed: 29152605]

Bostrom MM, Irjala H, Mirtti T, Taimen P, Kauko T, Algars A, Jalkanen S, and Bostrom PJ (2015). Tumor-Associated Macrophages Provide Significant Prognostic Information in Urothelial Bladder Cancer. PLoS One 10, e0133552. [PubMed: 26197470]

Bulla R, Tripodo C, Rami D, Ling GS, Agostinis C, Guarnotta C, Zorzet S, Durigutto P, Botto M, and Tedesco F (2016). C1q acts in the tumour microenvironment as a cancer-promoting factor independently of complement activation. Nat Commun 7, 10346. [PubMed: 26831747]

Chen Z, Wang GX, Ma SL, Jung DY, Ha H, Altamimi T, Zhao XY, Guo L, Zhang P, Hu CR, et al. (2017). Nrg4 promotes fuel oxidation and a healthy adipokine profile to ameliorate diet-induced metabolic disorders. Mol Metab 6, 863–872. [PubMed: 28752050]

Cohen JC, Horton JD, and Hobbs HH (2011). Human fatty liver disease: old questions and new insights. Science 332, 1519–1523. [PubMed: 21700865]

Collier JL, Weiss SA, Pauken KE, Sen DR, and Sharpe AH (2021). Not-so-opposite ends of the spectrum: CD8(+) T cell dysfunction across chronic infection, cancer and autoimmunity. Nat Immunol 22, 809–819. [PubMed: 34140679]

Comas F, Martinez C, Sabater M, Ortega F, Latorre J, Diaz-Saez F, Aragones J, Camps M, Guma A, Ricart W, et al. (2019). Neuregulin 4 Is a Novel Marker of Beige Adipocyte Precursor Cells in Human Adipose Tissue. Front Physiol 10, 39. [PubMed: 30766490]

Cortes M, Sanchez-Moral L, de Barrios O, Fernandez-Acenero MJ, Martinez-Campanario MC, Esteve-Codina A, Darling DS, Gyorffy B, Lawrence T, Dean DC, et al. (2017). Tumor-associated macrophages (TAMs) depend on ZEB1 for their cancer-promoting roles. EMBO J 36, 3336–3355. [PubMed: 29038174]

Dai YN, Zhu JZ, Fang ZY, Zhao DJ, Wan XY, Zhu HT, Yu CH, and Li YM (2015). A case-control study: Association between serum neuregulin 4 level and non-alcoholic fatty liver disease. Metabolism 64, 1667–1673. [PubMed: 26476959]

Dobie R, Wilson-Kanamori JR, Henderson BEP, Smith JR, Matchett KP, Portman JR, Wallenborg K, Picelli S, Zagorska A, Pendem SV, et al. (2019). Single-Cell Transcriptomics Uncovers Zonation of Function in the Mesenchyme during Liver Fibrosis. Cell Rep 29, 1832–1847 e1838. [PubMed: 31722201]

Dudek M, Pfister D, Donakonda S, Filpe P, Schneider A, Laschinger M, Hartmann D, Huser N, Meiser P, Bayerl F, et al. (2021). Auto-aggressive CXCR6(+) CD8 T cells cause liver immune pathology in NASH. Nature 592, 444–449. [PubMed: 33762736]

Efremova M, Vento-Tormo M, Teichmann SA, and Vento-Tormo R (2020). CellPhoneDB: inferring cell-cell communication from combined expression of multi-subunit ligand-receptor complexes. Nat Protoc 15, 1484–1506. [PubMed: 32103204]

Feng GS, Hanley KL, Liang Y, and Lin X (2021). Improving the Efficacy of Liver Cancer Immunotherapy: The Power of Combined Preclinical and Clinical Studies. Hepatology 73 Suppl 1, 104–114.

Friedman SL, Neuschwander-Tetri BA, Rinella M, and Sanyal AJ (2018). Mechanisms of NAFLD development and therapeutic strategies. Nat Med 24, 908–922. [PubMed: 29967350]

Giraud J, Chalopin D, Blanc JF, and Saleh M (2021). Hepatocellular Carcinoma Immune Landscape and the Potential of Immunotherapies. Front Immunol 12, 655697. [PubMed: 33815418]

Greten TF, Lai CW, Li G, and Staveley-O'Carroll KF (2019). Targeted and Immune-Based Therapies for Hepatocellular Carcinoma. Gastroenterology 156, 510–524. [PubMed: 30287171]

Guo L, Zhang P, Chen Z, Xia H, Li S, Zhang Y, Kobberup S, Zou W, and Lin JD (2017). Hepatic neuregulin 4 signaling defines an endocrine checkpoint for steatosis-to-NASH progression. J Clin Invest 127, 4449–4461. [PubMed: 29106384]

Halpern KB, Shenhav R, Massalha H, Toth B, Egozi A, Massasa EE, Medgalia C, David E, Giladi A, Moor AE, et al. (2018). Paired-cell sequencing enables spatial gene expression mapping of liver endothelial cells. Nat Biotechnol 36, 962–970. [PubMed: 30222169]

Halpern KB, Shenhav R, Matcovitch-Natan O, Toth B, Lemze D, Golan M, Massasa EE, Baydatch S, Landen S, Moor AE, et al. (2017). Single-cell spatial reconstruction reveals global division of labour in the mammalian liver. Nature 542, 352–356. [PubMed: 28166538]

Jaitin DA, Adlung L, Thaiss CA, Weiner A, Li B, Descamps H, Lundgren P, Bleriot C, Liu Z, Deczkowska A, et al. (2019). Lipid-Associated Macrophages Control Metabolic Homeostasis in a Trem2-Dependent Manner. Cell 178, 686–698 e614. [PubMed: 31257031]

Jiang J, Lin M, Xu Y, Shao J, Li X, Zhang H, and Yang S (2016). Circulating neuregulin 4 levels are inversely associated with subclinical cardiovascular disease in obese adults. Sci Rep 6, 36710. [PubMed: 27819316]

Katzenelenbogen Y, Sheban F, Yalin A, Yofe I, Svetlichnyy D, Jaitin DA, Bornstein C, Moshe A, Keren-Shaul H, Cohen M, et al. (2020). Coupled scRNA-Seq and Intracellular Protein Activity Reveal an Immunosuppressive Role of TREM2 in Cancer. Cell 182, 872–885 e819. [PubMed: 32783915]

Kawada N, Imanaka K, Kawaguchi T, Tamai C, Ishihara R, Matsunaga T, Gotoh K, Yamada T, and Tomita Y (2009). Hepatocellular carcinoma arising from non-cirrhotic nonalcoholic steatohepatitis. J Gastroenterol 44, 1190–1194. [PubMed: 19672551]

Klemke L, De Oliveira T, Witt D, Winkler N, Bohnenberger H, Bucala R, Conradi LC, and Schulz-Heddergott R (2021). Hsp90-stabilized MIF supports tumor progression via macrophage recruitment and angiogenesis in colorectal cancer. Cell Death Dis 12, 155. [PubMed: 33542244]

Krenkel O, Hundertmark J, Abdallah AT, Kohlhepp M, Puengel T, Roth T, Branco DPP, Mossanen JC, Luedde T, Trautwein C, et al. (2020). Myeloid cells in liver and bone marrow acquire a functionally distinct inflammatory phenotype during obesity-related steatohepatitis. Gut 69, 551–563. [PubMed: 31076404]

La Manno G, Soldatov R, Zeisel A, Braun E, Hochgerner H, Petukhov V, Lidschreiber K, Kastriti ME, Lonnerberg P, Furlan A, et al. (2018). RNA velocity of single cells. Nature 560, 494–498. [PubMed: 30089906]

Li S, Liu C, Li N, Hao T, Han T, Hill DE, Vidal M, and Lin JD (2008). Genome-wide coactivation analysis of PGC-1alpha identifies BAF60a as a regulator of hepatic lipid metabolism. Cell Metab 8, 105–117. [PubMed: 18680712]

Li Y, Jin L, Jiang F, Yan J, Lu Y, Yang Q, Zhang Y, Zhang H, Yu H, Zhang Y, et al. (2021). Mutations of NRG4 contribute to the pathogenesis of non-alcoholic fatty liver disease and related metabolic disorders. Diabetes.

Liu Y, Song L, Ni H, Sun L, Jiao W, Chen L, Zhou Q, Shen T, Cui H, Gao T, et al. (2017). ERBB4 acts as a suppressor in the development of hepatocellular carcinoma. Carcinogenesis 38, 465–473. [PubMed: 28334319]

Loomba R, Friedman SL, and Shulman GI (2021). Mechanisms and disease consequences of nonalcoholic fatty liver disease. Cell 184, 2537–2564. [PubMed: 33989548]

Ludwig J, Viggiano TR, McGill DB, and Oh BJ (1980). Nonalcoholic steatohepatitis: Mayo Clinic experiences with a hitherto unnamed disease. Mayo Clin Proc 55, 434–438. [PubMed: 7382552]

MacParland SA, Liu JC, Ma XZ, Innes BT, Bartczak AM, Gage BK, Manuel J, Khuu N, Echeverri J, Linares I, et al. (2018). Single cell RNA sequencing of human liver reveals distinct intrahepatic macrophage populations. Nat Commun 9, 4383. [PubMed: 30348985]

Magrini E, Di Marco S, Mapelli SN, Perucchini C, Pasqualini F, Donato A, de la Luz Guevara Lopez M, Carriero R, Ponzetta A, Colombo P, et al. (2021). Complement activation promoted by

the lectin pathway mediates C3aR-dependent sarcoma progression and immunosuppression. Nat Cancer 2, 218–232. [PubMed: 34505065]

Marengo A, Rosso C, and Bugianesi E (2016). Liver Cancer: Connections with Obesity, Fatty Liver, and Cirrhosis. Annu Rev Med 67, 103–117. [PubMed: 26473416]

Matsumoto M, Hada N, Sakamaki Y, Uno A, Shiga T, Tanaka C, Ito T, Katsume A, and Sudoh M (2013). An improved mouse model that rapidly develops fibrosis in non-alcoholic steatohepatitis. Int J Exp Pathol 94, 93–103. [PubMed: 23305254]

McLane LM, Abdel-Hakeem MS, and Wherry EJ (2019). CD8 T Cell Exhaustion During Chronic Viral Infection and Cancer. Annu Rev Immunol 37, 457–495. [PubMed: 30676822]

Mederacke I, Dapito DH, Affo S, Uchinami H, and Schwabe RF (2015). High-yield and high-purity isolation of hepatic stellate cells from normal and fibrotic mouse livers. Nat Protoc 10, 305–315. [PubMed: 25612230]

Medler TR, Murugan D, Horton W, Kumar S, Cotechini T, Forsyth AM, Leyshock P, Leitenberger JJ, Kulesz-Martin M, Margolin AA, et al. (2018). Complement C5a Fosters Squamous Carcinogenesis and Limits T Cell Response to Chemotherapy. Cancer Cell 34, 561–578 e566. [PubMed: 30300579]

Mohamad B, Shah V, Onyshchenko M, Elshamy M, Aucejo F, Lopez R, Hanouneh IA, Alhaddad R, and Alkhouri N (2016). Characterization of hepatocellular carcinoma (HCC) in non-alcoholic fatty liver disease (NAFLD) patients without cirrhosis. Hepatol Int 10, 632–639. [PubMed: 26558795]

Molawi K, and Sieweke MH (2015). Monocytes compensate Kupffer cell loss during bacterial infection. Immunity 42, 10–12. [PubMed: 25607453]

Molgora M, Esaulova E, Vermi W, Hou J, Chen Y, Luo J, Brioschi S, Bugatti M, Omodei AS, Ricci B, et al. (2020). TREM2 Modulation Remodels the Tumor Myeloid Landscape Enhancing Anti-PD-1 Immunotherapy. Cell 182, 886–900 e817. [PubMed: 32783918]

Mulder K, Patel AA, Kong WT, Piot C, Halitzki E, Dunsmore G, Khalilnezhad S, Irac SE, Dubuisson A, Chevrier M, et al. (2021). Cross-tissue single-cell landscape of human monocytes and macrophages in health and disease. Immunity 54, 1883–1900 e1885. [PubMed: 34331874]

Obradovic A, Chowdhury N, Haake SM, Ager C, Wang V, Vlahos L, Guo XV, Aggen DH, Rathmell WK, Jonasch E, et al. (2021). Single-cell protein activity analysis identifies recurrence-associated renal tumor macrophages. Cell 184, 2988–3005 e2916. [PubMed: 34019793]

Pfister D, Nunez NG, Pinyol R, Govaere O, Pinter M, Szydlowska M, Gupta R, Qiu M, Deczkowska A, Weiner A, et al. (2021). NASH limits anti-tumour surveillance in immunotherapy-treated HCC. Nature 592, 450–456. [PubMed: 33762733]

Pilotto A, Padovani A, and Network E-B (2020). Reply to the Letter "COVID-19-Associated Encephalopathy and Cytokine-Mediated Neuroinflammation". Ann Neurol 88, 861–862. [PubMed: 32737995]

Ramachandran P, Dobie R, Wilson-Kanamori JR, Dora EF, Henderson BEP, Luu NT, Portman JR, Matchett KP, Brice M, Marwick JA, et al. (2019). Resolving the fibrotic niche of human liver cirrhosis at single-cell level. Nature 575, 512–518. [PubMed: 31597160]

Ramachandran P, Matchett KP, Dobie R, Wilson-Kanamori JR, and Henderson NC (2020). Single-cell technologies in hepatology: new insights into liver biology and disease pathogenesis. Nat Rev Gastroenterol Hepatol 17, 457–472. [PubMed: 32483353]

Rosenthal SB, Liu X, Ganguly S, Dhar D, Pasillas MP, Ricciardelli E, Li RZ, Troutman TD, Kisseleva T, Glass CK, et al. (2021). Heterogeneity of HSCs in a Mouse Model of NASH. Hepatology 74, 667–685. [PubMed: 33550587]

Rui L, and Lin JD (2022). Reprogramming of Hepatic Metabolism and Microenvironment in Nonalcoholic Steatohepatitis. Annu Rev Nutr.

Sangro B, Sarobe P, Hervas-Stubbs S, and Melero I (2021). Advances in immunotherapy for hepatocellular carcinoma. Nat Rev Gastroenterol Hepatol 18, 525–543. [PubMed: 33850328]

Schumacher MA, Dennis IC, Liu CY, Robinson C, Shang J, Bernard JK, Washington MK, Polk DB, and Frey MR (2021). NRG4-ErbB4 signaling represses proinflammatory macrophage activity. Am J Physiol Gastrointest Liver Physiol 320, G990–G1001. [PubMed: 33826403]

Schumacher MA, Hedl M, Abraham C, Bernard JK, Lozano PR, Hsieh JJ, Almohazey D, Bucar EB, Punit S, Dempsey PJ, et al. (2017). ErbB4 signaling stimulates pro-inflammatory macrophage apoptosis and limits colonic inflammation. Cell Death Dis 8, e2622. [PubMed: 28230865]

Segers VFM, Dugaucquier L, Feyen E, Shakeri H, and De Keulenaer GW (2020). The role of ErbB4 in cancer. Cell Oncol (Dordr) 43, 335–352. [PubMed: 32219702]

Seidman JS, Troutman TD, Sakai M, Gola A, Spann NJ, Bennett H, Bruni CM, Ouyang Z, Li RZ, Sun X, et al. (2020). Niche-Specific Reprogramming of Epigenetic Landscapes Drives Myeloid Cell Diversity in Nonalcoholic Steatohepatitis. Immunity 52, 1057–1074 e1057. [PubMed: 32362324]

Shalapour S, and Karin M (2020). Cruel to Be Kind: Epithelial, Microbial, and Immune Cell Interactions in Gastrointestinal Cancers. Annu Rev Immunol 38, 649–671. [PubMed: 32040356]

Sharma A, Seow JJW, Dutertre CA, Pai R, Bleriot C, Mishra A, Wong RMM, Singh GSN, Sudhagar S, Khalilnezhad S, et al. (2020). Onco-fetal Reprogramming of Endothelial Cells Drives Immunosuppressive Macrophages in Hepatocellular Carcinoma. Cell 183, 377–394 e321. [PubMed: 32976798]

Sheka AC, Adeyi O, Thompson J, Hameed B, Crawford PA, and Ikramuddin S (2020). Nonalcoholic Steatohepatitis: A Review. JAMA 323, 1175–1183. [PubMed: 32207804]

Stuart T, Butler A, Hoffman P, Hafemeister C, Papalexi E, Mauck WM 3rd, Hao Y, Stoeckius M, Smibert P, and Satija R (2019). Comprehensive Integration of Single-Cell Data. Cell 177, 1888–1902 e1821. [PubMed: 31178118]

Suzuki A, and Diehl AM (2017). Nonalcoholic Steatohepatitis. Annu Rev Med 68, 85–98. [PubMed: 27732787]

Tacke F, and Zimmermann HW (2014). Macrophage heterogeneity in liver injury and fibrosis. J Hepatol 60, 1090–1096. [PubMed: 24412603]

Tutunchi H, Ostadrahimi A, Hosseinzadeh-Attar MJ, Miryan M, Mobasseri M, and Ebrahimi-Mameghani M (2020). A systematic review of the association of neuregulin 4, a brown fat-enriched secreted factor, with obesity and related metabolic disturbances. Obes Rev 21, e12952. [PubMed: 31782243]

Ulland TK, Song WM, Huang SC, Ulrich JD, Sergushichev A, Beatty WL, Loboda AA, Zhou Y, Cairns NJ, Kambal A, et al. (2017). TREM2 Maintains Microglial Metabolic Fitness in Alzheimer's Disease. Cell 170, 649–663 e613. [PubMed: 28802038]

Wan S, Kuo N, Kryczek I, Zou W, and Welling TH (2015). Myeloid cells in hepatocellular carcinoma. Hepatology 62, 1304–1312. [PubMed: 25914264]

Wang GX, Zhao XY, Meng ZX, Kern M, Dietrich A, Chen Z, Cozacov Z, Zhou D, Okunade AL, Su X, et al. (2014). The brown fat-enriched secreted factor Nrg4 preserves metabolic homeostasis through attenuation of hepatic lipogenesis. Nat Med 20, 1436–1443. [PubMed: 25401691]

Wang R, Yang F, Qing L, Huang R, Liu Q, and Li X (2019). Decreased serum neuregulin 4 levels associated with non-alcoholic fatty liver disease in children with obesity. Clin Obes 9, e12289. [PubMed: 30411515]

Wen L, Xin B, Wu P, Lin CH, Peng C, Wang G, Lee J, Lu LF, and Feng GS (2019). An Efficient Combination Immunotherapy for Primary Liver Cancer by Harmonized Activation of Innate and Adaptive Immunity in Mice. Hepatology 69, 2518–2532. [PubMed: 30693544]

Wherry EJ, and Kurachi M (2015). Molecular and cellular insights into T cell exhaustion. Nat Rev Immunol 15, 486–499. [PubMed: 26205583]

Wolf MJ, Adili A, Piotrowitz K, Abdullah Z, Boege Y, Stemmer K, Ringelhan M, Simonavicius N, Egger M, Wohlleber D, et al. (2014). Metabolic activation of intrahepatic CD8+ T cells and NKT cells causes nonalcoholic steatohepatitis and liver cancer via cross-talk with hepatocytes. Cancer Cell 26, 549–564. [PubMed: 25314080]

Xiong X, Kuang H, Ansari S, Liu T, Gong J, Wang S, Zhao XY, Ji Y, Li C, Guo L, et al. (2019a). Landscape of Intercellular Crosstalk in Healthy and NASH Liver Revealed by Single-Cell Secretome Gene Analysis. Mol Cell 75, 644–660 e645. [PubMed: 31398325]

Xiong X, Kuang H, Liu T, and Lin JD (2020). A single-cell perspective of the mammalian liver in health and disease. Hepatology.

Xiong X, Wang Q, Wang S, Zhang J, Liu T, Guo L, Yu Y, and Lin JD (2019b). Mapping the molecular signatures of diet-induced NASH and its regulation by the hepatokine Tsukushi. Mol Metab 20, 128–137. [PubMed: 30595550]

Zhang P, Kuang H, He Y, Idiga SO, Li S, Chen Z, Yang Z, Cai X, Zhang K, Potthoff MJ, et al. (2018). NRG1-Fc improves metabolic health via dual hepatic and central action. JCI Insight 3.

Zhang Q, He Y, Luo N, Patel SJ, Han Y, Gao R, Modak M, Carotta S, Haslinger C, Kind D, et al. (2019). Landscape and Dynamics of Single Immune Cells in Hepatocellular Carcinoma. Cell 179, 829–845 e820. [PubMed: 31675496]

Zheng C, Zheng L, Yoo JK, Guo H, Zhang Y, Guo X, Kang B, Hu R, Huang JY, Zhang Q, et al. (2017). Landscape of Infiltrating T Cells in Liver Cancer Revealed by Single-Cell Sequencing. Cell 169, 1342–1356 e1316. [PubMed: 28622514]

Highlights

- NASH induces TAM-like macrophages and T cell exhaustion in the liver
- The NRG4 hormonal axis restrains the tumor-prone liver immune microenvironment in NASH
- NRG4 functions as a tumor suppressor for NASH-associated liver cancer
- Recombinant NRG4 fusion protein is highly potent in suppressing NASH-HCC

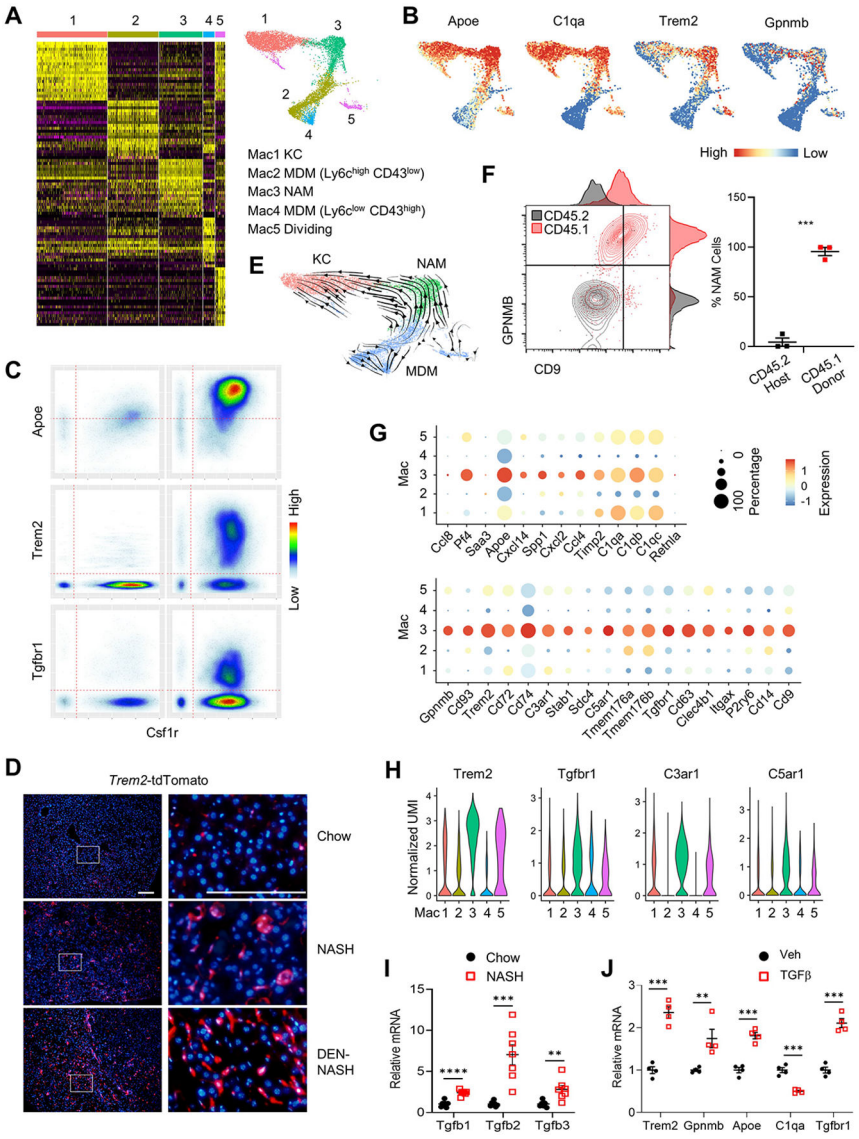

Figure 1. Induction and regulation of TAM-like macrophages in NASH liver.

(A) Heatmap of top 20 marker genes for the macrophage subclusters.

(B) Feature plots illustrating macrophage gene expression.

(C) Virtual flow analysis of intrahepatic macrophages by gating for Csf1r and Apoe, Trem2, or Tgfbr1 mRNA expression.

(D) Fluorescence images of liver sections from Trem2-Cre/Rosa26-tdTomato mice under different treatment conditions. Scale bars represent 100μm.

(E) RNA velocity analysis of macrophage gene expression. Arrows denote likely trajectory of cell states among different subpopulations.

(F) Flow cytometry analysis of liver macrophages in mice fed NASH diet following bone marrow transplantation.

(G) Bubble plot illustrating relative mRNA expression for genes encoding secreted factors (top) and membrane proteins (bottom) with enriched expression in NAMs.

(H) Violin plot of gene expression among different macrophage subclusters.

(I) qPCR analysis of Tgfb expression in chow and NASH liver.

(J) qPCR analysis of gene expression in cultured BMDMs treated with vehicle or 2.5 ng/ml TGFβ for 24 hrs.

Data in (F), (I), and (J) represent mean ± SEM; two-tailed unpaired Student's *t*-test. **p<0.01, ***p<0.001, ****p<0.0001.

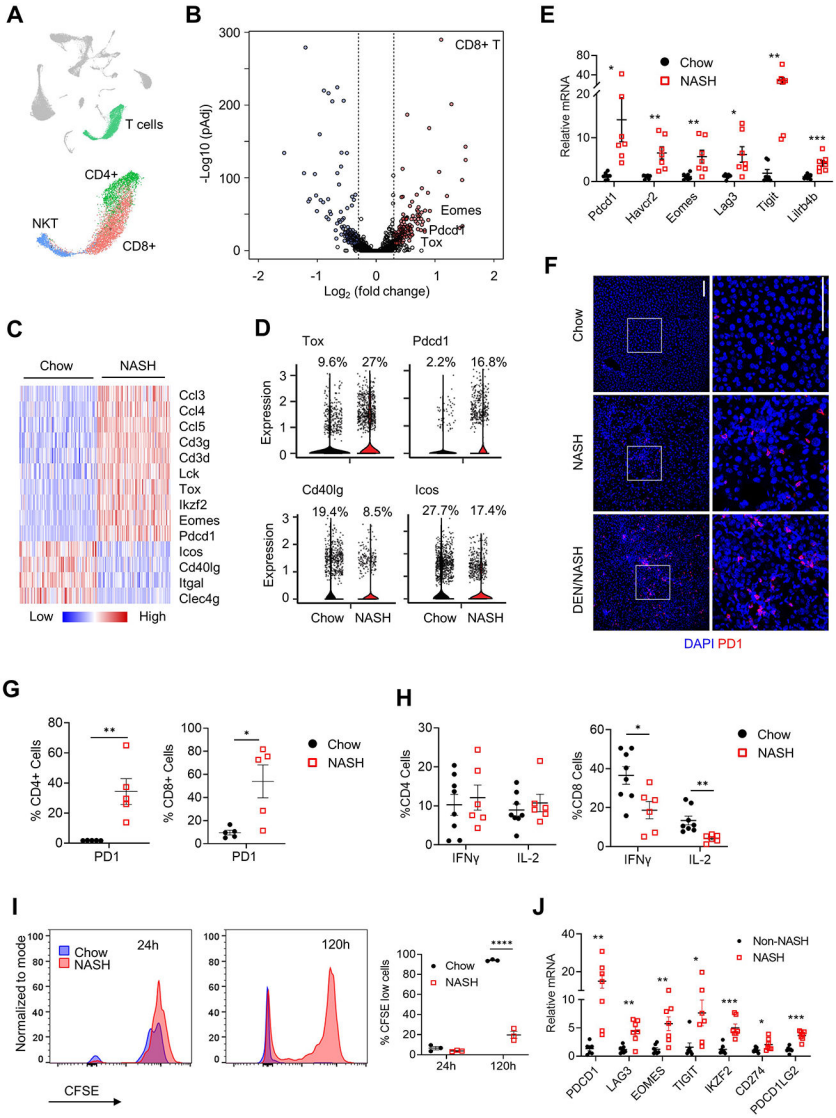

Figure 2. NASH pathogenesis triggers CD8+ T cell exhaustion in the liver.

(A) UMAP illustrating T cells among liver NPCs (top) and three T cell subclusters (bottom).

(B) Volcano plot of gene expression using averaged values of normalized expression levels for CD8+ T cells from chow and NASH livers. X-axis indicates log-transformed fold change of gene expression between NASH and chow livers.

(C) Heatmap of a subset of genes differentially expressed in CD8+ T cells from chow and NASH mouse livers.

(D) Dot plot illustrating relative abundance of CD8+ T cells expressing Cd8a in combination with the indicated genes in chow and NASH livers.

(E) qPCR analysis of hepatic gene expression in mice fed chow (n=7) or NASH (n=7) diet for 4 months.

(F) Confocal images of anti-PD1 immunofluorescence staining on liver sections. Scale bars=10μm.

(G) Flow cytometry analysis of PD1 expression in intrahepatic T cells from mice fed chow (n=5) and NASH (n=5) diet.
(H) Flow cytometry analysis of intracellular IFNγ and IL-2. Liver NPCs from mice fed chow (n=8) or NASH (n=6) diet for 5 months were treated with PMA/ionomycin for 6 hrs.
(I) CFSE proliferation assay of CD8+ T cells. NPCs from chow (n=3) or NASH (n=3) mouse livers were incubated with CD3/CD28 Dynabeads for 24 and 120 hrs.
(J) qPCR analysis of gene expression in liver biopsies from non-NASH (n=7) and NASH patients (n=7).
Data in (E), (G), (H), (I) and (J) represent mean ± SEM; two-tailed unpaired Student's *t*-test. *p<0.05, **p<0.01, ***p<0.001, ****p<0.0001.

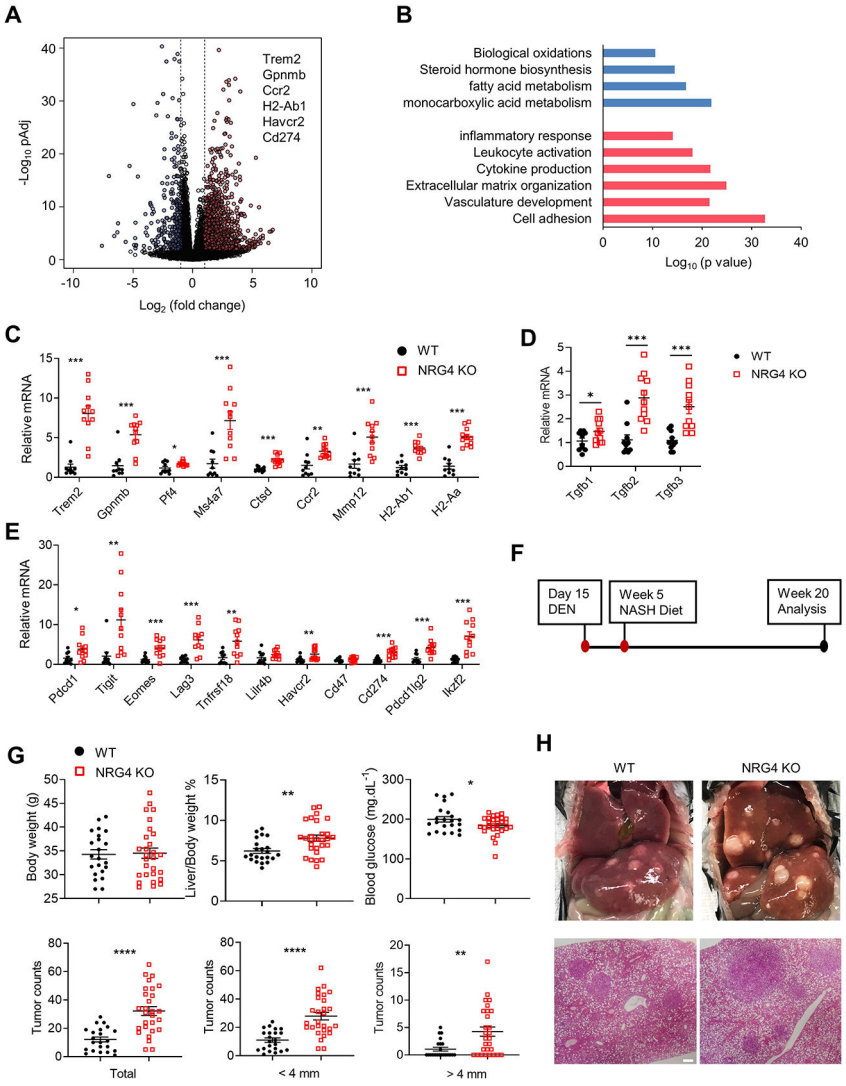

Figure 3. NRG4 serves as a hormonal checkpoint for NASH-associated HCC.

(A) Volcano plot illustrating differential gene expression. Bulk liver RNA sequencing was performed on three pairs of pooled NASH diet-fed WT and NRG4 KO mice. X-axis indicates log-transformed fold change of gene expression between KO and WT mice.

(B) Gene ontology analysis of upregulated (red) and downregulated (blue) genes in (A).

(C) qPCR analysis of hepatic gene expression in WT (n=10) and NRG4 KO (n=11) mice fed NASH diet for 6 months.

(D) A schematic outline of DEN/NASH liver tumor study using male WT (n=22) and NRG4 KO (n=28) mice. NASH diet feeding was initiated at 5 weeks of age.

(E) Metabolic parameters and tumor count in WT (n=22) and NRG4 KO (n=28) mice subjected to the DEN/NASH protocol.

(F) A schematic outline of DEN/NASH liver tumor study using male WT (n=22) and NRG4 KO (n=28) mice. NASH diet feeding was initiated at 5 weeks of age.

(G) Metabolic parameters and tumor count in the treated mice.

(H) Liver appearance and histology. Scale bar=20μm.

Data in (C), (D), (E) and (G) represent mean ± SEM; two-tailed unpaired Student's *t*-test. *p<0.05, **p<0.01, ***p<0.001, ****p<0.0001.

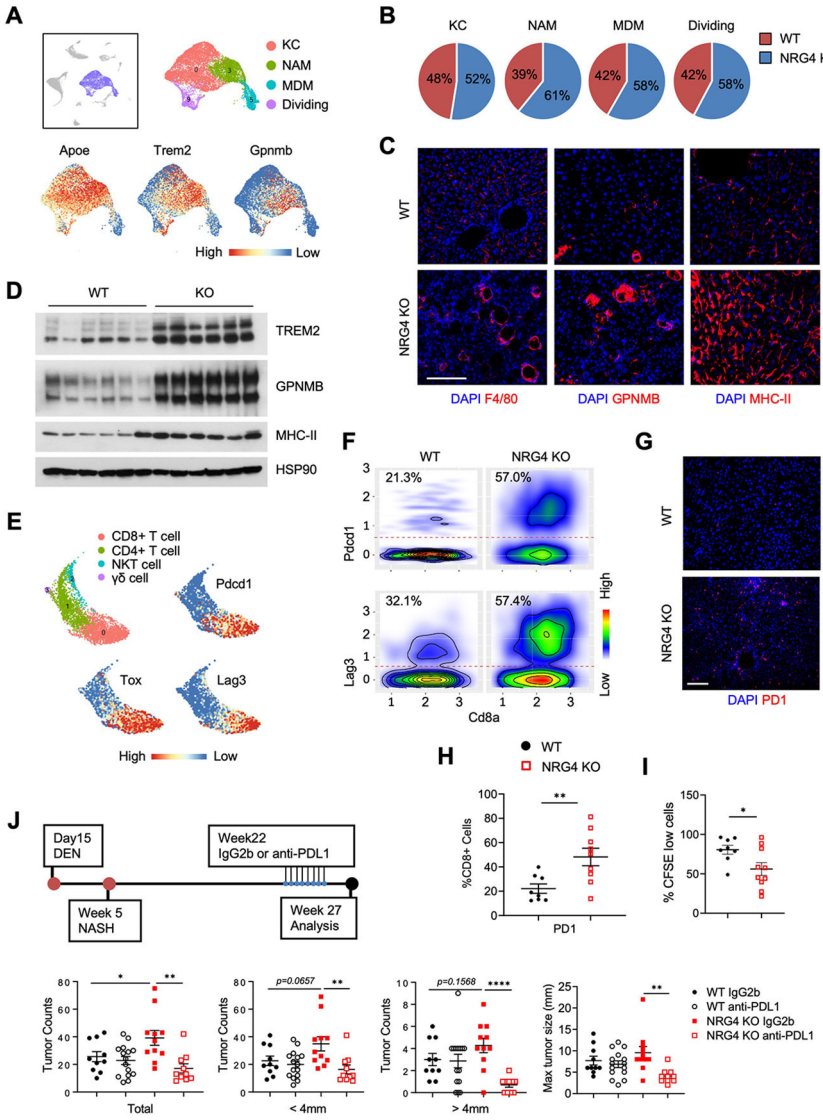

Figure 4. Effects of NRG4 deficiency on the liver immune microenvironment.

Single-cell RNAseq analysis of liver NPCs isolated from WT (n=4) and Nrg4 KO (n=4) mice following 7 months of NASH diet feeding.

(A) Macrophage subclusters and feature plots.

(B) Pie chart of macrophage cell count from WT (red) and NRG4 KO (blue) livers in each subcluster.

(C) Confocal images of liver immunofluorescence staining. Scale bar=10μm.

(D) Immunoblots of total liver lysates from WT and NRG4 KO mice fed NASH diet for 6 months.

(E) T cell subclusters and feature plots.

(F) Virtual flow analysis of intrahepatic CD8+ T cells by gating for Cd8a in combination with Pdcd1 or Lag3 mRNA levels.

(G) Confocal images of liver immunofluorescence staining. Scale bar=10μm.

(H) Flow cytometry analysis of PD1 expression in intrahepatic CD8+ T cells from NASH diet fed WT (n=8) and NRG4 KO (n=9) mice.
(I) CFSE proliferation assay of CD8+ T cells from WT (n=8) and NRG4 KO (n=10) mice fed NASH diet for 5 months.
(J) Anti-PDL1 treatment study. WT and NRG4 KO mice were subjected to the DEN/NASH tumor induction protocol followed by treatments twice a week: WT IgG2b (n=10), WT anti-PDL1 (n=15), Nrg4 KO IgG2b (n=11), Nrg4 KO anti-PDL1 (n=10).
Data in (G), (I) and (J) represent mean ± SEM; two-tailed unpaired Student's *t*-test. *p<0.05, **p<0.01, and ****p<0.0001.

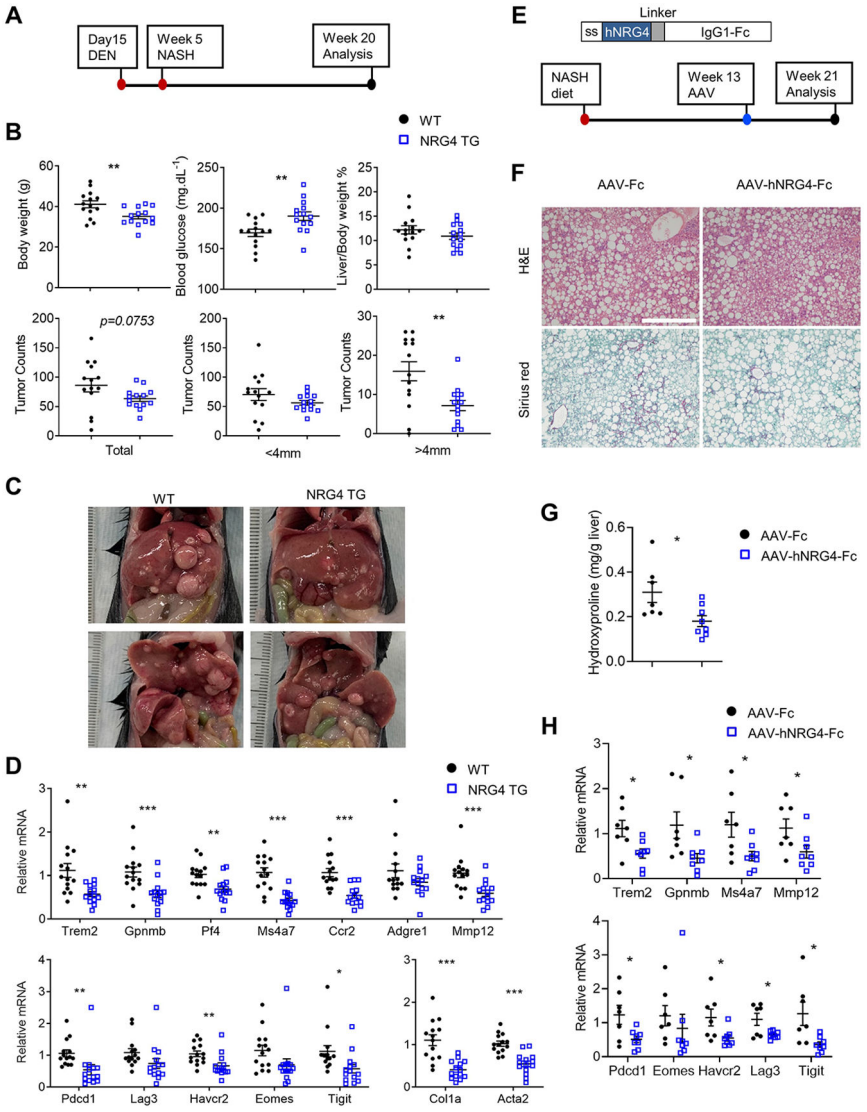

Figure 5. Inhibition of tumor-prone liver microenvironment and NASH-HCC by NRG4.

(A) A schematic overview of DEN/NASH liver tumor study using male WT (n=14) and NRG4 TG (n=14) mice. NASH diet feeding was initiated at 5 weeks of age.

(B) Metabolic parameters and tumor count in treated mice.

(C) Liver appearance.

(D) qPCR analysis of gene expression WT and NRG4 TG mouse livers.

(E) A schematic diagram of hNRG4-Fc fusion protein design and study outline.

(F) H&E histology and Sirius red staining of liver sections from transduced mice. Scale bar=20μm.

(G) Liver hydroxyproline content in mice transduced with AAV-Fc (n=7) or AAV-hNRG4-Fc (n=8).

(H) qPCR analysis of hepatic gene expression in transduced mice.

Data in (B), (D), (G) and (H) represent mean ± SEM; two-tailed unpaired Student's *t*-test. *p<0.05, **p<0.01, ***p<0.001.

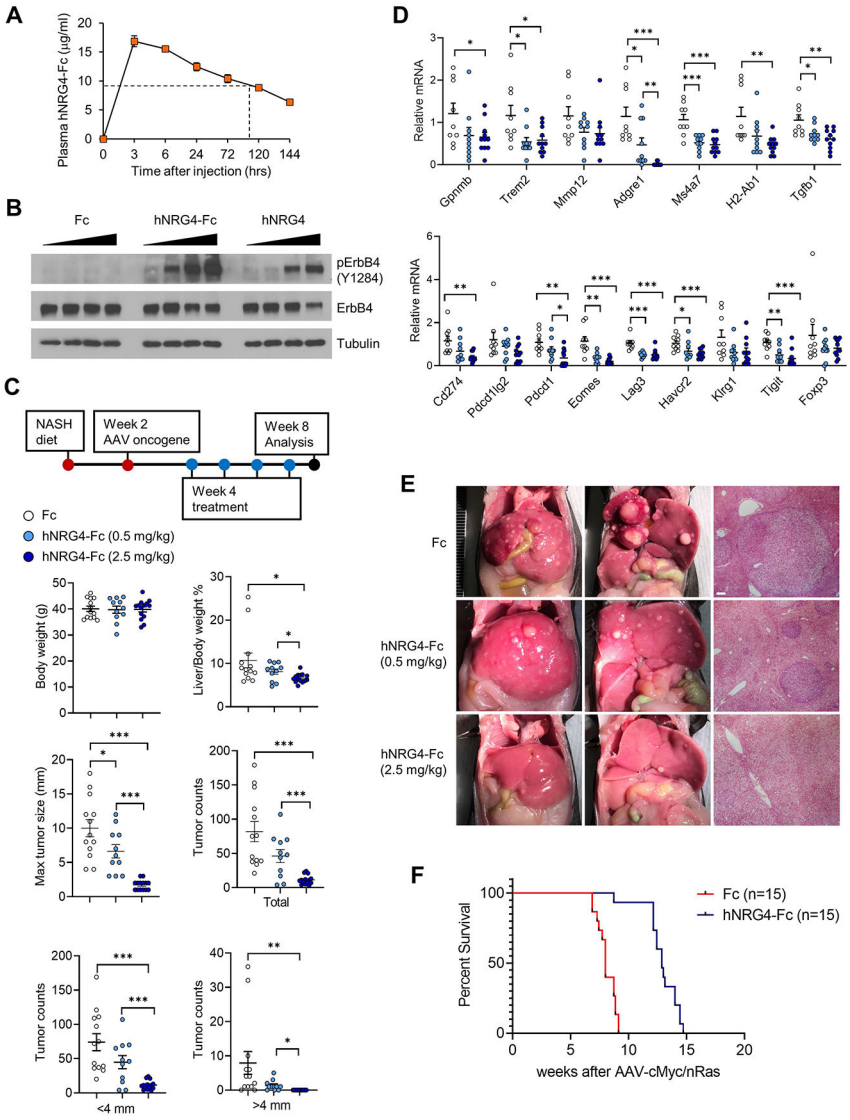

Figure 6. Suppression of oncogene-induced HCC by recombinant hNRG4-Fc fusion protein.

(A) Plasma concentrations of hNRG4-Fc, as measured by hIgG1 Fc ELISA, at different time points following a single injection of the fusion protein (2 mg/kg, i.p.).

(B) Immunoblots of total Min6 cell lysates treated with Fc, hNRG4-Fc, or hNRG4 peptide at 0.8, 4, 20, or 100 nM for 15 minutes.

(C) A schematic outline of hNRG4-Fc fusion protein treatment study, and the metabolic parameters and tumor burden in the treated mice. Four-month-old male mice were transduced with AAV-cMYC/AAV-nRAS followed by weekly treatment with Fc (2.5 mg/kg, n=13) or hNRG4-Fc at 0.5 mg/kg (n=11) or 2.5 mg/kg (n=14).

(D) qPCR analysis of hepatic gene expression in treated mice.

(E) Liver appearance and histology. Scale bar=200μm.

(F) Survival curves of transduced mice treated with 1.5 mg/kg of Fc (n=15) or hNRG4-Fc (n=15) fusion protein.

Data in (C) and (D) represent mean ± SEM; two-tailed unpaired Student's *t*-test. *p<0.05, **p<0.01, ***p<0.001.

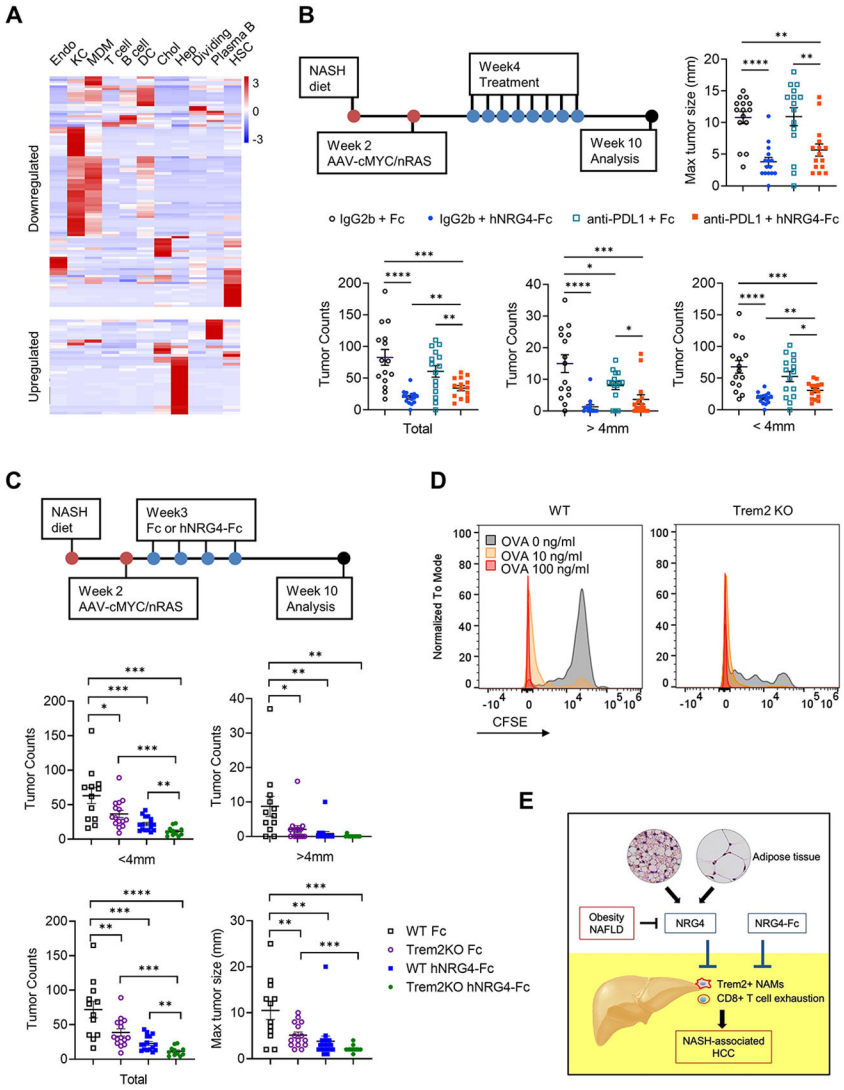

Figure 7. Interaction between NRG4 and the liver immune microenvironment in NASH-HCC.

(A) Heatmap illustrating expression patterns of NRG4-regulated genes among different liver cell types.

(B) hNRG4-Fc and anti-PDL1 co-treatment study. WT male mice transduced with AAV oncogenes were randomly divided into four treatment groups: IgG2b+Fc (n=15), IgG2b+hNRG4-Fc (n=15), anti-PDL1+Fc (n=15), anti-PDL1+hNRG4-Fc (n=15).

(C) Tumor burden in transduced WT and Trem2 KO mice: WT Fc (n=12), Trem2KO Fc (n=15), WT hNRG4-Fc (n=16), Trem2KO hNRG4-Fc (n=11).

(D) CFSE proliferation assay of splenic CD8+ T cells from OT-1 transgenic mice co-cultured with BMDMs from WT and Trem2 KO mice in the absence or presence of OVA.

(E) A model depicting NRG4 as a hormonal checkpoint in NASH-associated HCC.

Data in (B) and (C) represent mean ± SEM; two-tailed unpaired Student's *t*-test. *p<0.05, **p<0.01, ***p<0.001, ****p<0.0001.

KEY RESOURCES TABLE

REAGENT or RESOURCE	SOURCE	IDENTIFIER
Antibodies		
anti-Trem2	Dr. Marco Colonna	N/A
anti-Gpnmb	R&D	AF2330
anti-MHC-II	Invitrogen	14-5321-85
anti-HSP90	Santa Cruz	Sc-13119
anti-β-tubulin	Santa Cruz	Sc-32293
anti-Fc	Invitrogen	A10648
anti-CD8	Invitrogen	14-0808-82
anti-F4/80	Bio-RAD	MCA497G
anti-PD1	R&D	AF1021
anti-Rat IgG (H+L) Cross-Adsorbed Secondary Antibody, Alexa Fluor™ 594	Invitrogen	A11007
Alexa Fluor® 488 AffiniPure Donkey Anti-Goat IgG (H+L)	Jackson ImmunoResearch	705-545-003
anti-human polyvalent immunoglobulins antibody	Sigma	I1761
HRP-conjugated goat anti-human IgG (Fc specific)	Sigma	A0170
anti-phospho-ErbB4(Y1284)	Cell Signaling Technology	4757
anti-ErbB4	Cell Signaling Technology	4795
Brilliant Violet 421™ anti-mouse CD45.2 Antibody	Biolegend	109831
Brilliant Violet 510™ anti-mouse CD45.1 Antibody	Biolegend	110741
Pacific Blue™ anti-mouse CD45 Antibody	Biolegend	103126
PE/Cyanine7 anti-mouse F4/80 Antibody	Biolegend	123114
PerCP/Cyanine5.5 anti-mouse/human CD11b Antibody	Biolegend	101227
PE anti-mouse CD9 Antibody	Biolegend	124805
Brilliant Violet 510™ anti-mouse CD90.2 Antibody	Biolegend	105335
PE anti-mouse CD4 Antibody	Biolegend	100407
PerCP/Cyanine5.5 anti-mouse CD8a Antibody	Biolegend	100734
Brilliant Violet 421™ anti-mouse CD279 (PD-1) Antibody	Biolegend	135218
PE anti-mouse IL-2 Antibody	Biolegend	503807
Alexa Fluor® 647 anti-mouse IFN-γ Antibody	Biolegend	505814
GPNMB Monoclonal Antibody (CTSREVL), eFluor™ 660	Thermo Fisher	50-5708-82
InVivoMAb rat IgG2b isotype control	BioXCell	BE0090
InVivoMAb anti-mouse PD-L1 (B7-H1)	BioXCell	BE0101
Bacterial and virus strains		
Stabl3 Competent cells	Invitrogen	C737303
BL21 Competent cells	Invitrogen	C600003
Biological samples		
Human NASH liver sample	Liver Tissue Cell Distribution System at the University of Minnesota (Guo et al., 2017)	

REAGENT or RESOURCE	SOURCE	IDENTIFIER
Chemicals, peptides, and recombinant proteins		
Pronase	Sigma	P5147
Collagenase type II	Worthington	LS004196
Collagenase type IV	Worthington	LS004188
DNase I	Roche	R104159001
Optiprep	Cosmo Bio USA	AXS-1114542-5
DAPI	Invitrogen	10236276001
TGF-beta	Thermo Fisher	50 112 2731
N-Nitrosodiethylamine (DEN)	Sigma	442687
Brefeldin A	Biolegend	420601
PMA/ionomycin	Biolegend	423302
Genemed Synthesis Ovalbumin (257-264)	Thermo Fisher	NC1901847
Recombinant Mouse M-CSF (carrier-free)	Biolegend	576406
Critical commercial assays		
CFSE Cell Division Tracker Kit	Biolegend	423801
Hydroxyproline Colorimetric Assay Kit	BioVision	K555-100
Stanbio Cholesterol kit	Thermo Fisher	SB-1010-430
ExpiFectamine™ 293 Transfection Kit	Thermo Fisher	A14525
Serum Triglyceride Determination Kit	Sigma	TR0100-1KT
Deposited data		
All RNA-seq data	This paper	GSE185042
WB data	This paper	
Experimental models: Cell lines		
Min6	Dr. Peter Dempsey (University of Colorado)	N/A
Expi293F™ Cells	Thermo Fisher	A14527
Experimental models: Organisms/strains		
C57BL/6J	Jackson Laboratory	JAX: 000664
td-Tomato	Dr. Jun Wu lab, University of Michigan	N/A
Nrg4 KO mice	Our lab	N/A
Nrg4 TG mice	Our lab	N/A
Trem2-Cre	Our lab	N/A
Oligonucleotides		
ms Tgfb1	Table S5	N/A
ms Tgfb2	Table S5	N/A
ms Tgfb3	Table S5	N/A
ms Trem2	Table S5	N/A
ms Gpnmb	Table S5	N/A
ms Apoe	Table S5	N/A
ms C1qa	Table S5	N/A

REAGENT or RESOURCE	SOURCE	IDENTIFIER
ms Tgfbr1	Table S5	N/A
ms Col1a	Table S5	N/A
ms Mmp13	Table S5	N/A
ms Mmp12	Table S5	N/A
ms Pdcd1	Table S5	N/A
ms Cd274	Table S5	N/A
ms Pdcd1lg2	Table S5	N/A
ms Havcr2	Table S5	N/A
ms Eomes	Table S5	N/A
ms Lag3	Table S5	N/A
ms Tigit	Table S5	N/A
ms Lilrb4b	Table S5	N/A
ms Tnfrsf18	Table S5	N/A
ms Cd47	Table S5	N/A
ms Ikzf2	Table S5	N/A
ms Ctsd	Table S5	N/A
ms Ccr2	Table S5	N/A
ms H2-Ab1	Table S5	N/A
ms H2-Aa	Table S5	N/A
ms Ms4a7	Table S5	N/A
ms Pf4	Table S5	N/A
ms Adgre1	Table S5	N/A
ms Acta2	Table S5	N/A
ms Klrg1	Table S5	N/A
ms Foxp3	Table S5	N/A
h PDCD1	Table S5	N/A
h LAG3	Table S5	N/A
h EOMES	Table S5	N/A
h TIGIT	Table S5	N/A
h IKZF2	Table S5	N/A
h CD274	Table S5	N/A
h PDCD1LG2	Table S5	N/A
Recombinant DNA		
AAV-CAG-Fc (Rc2/8)	This paper	N/A
AAV-CAG-hNRG4-Fc (Rc2/8)	This paper	N/A
AAV-TBG-cMyc (Rc2/8)	This paper	N/A
AAV-TBG-nRas (Rc2/8)	This paper	N/A
pcDNA3-Fc	This paper	N/A
pcDNA3-hNRG4-Fc	This paper	N/A

REAGENT or RESOURCE	SOURCE	IDENTIFIER
Software and algorithms		
FlowJo v10	Tree Star	N/A
R	Version 4.2.0	N/A
Seurat	Version 3.1.2	N/A
CellPhoneDB	V3	N/A
BiomaRt	Version 2.52.0	N/A
scVelo	Version 0.2.2	N/A
Attune™ NxT Software	Thermo Fisher	N/A
Python	Version 3.8.3	N/A
LAS X Life Science Microscope Software	Leica	N/A
GraphPad Prizm9.0	Dotmatics	N/A
Other		
Standard chow	Teklad	5001 Laboratory Diet
NASH Diet	Research Diets	D09100310
Transcription factor staining buffer set	Invitrogen	50-112-8857
Gibco™ Dynabeads™ Mouse T-Activator CD3/CD28	Thermo Fisher	11-452-D
Ultra TMB-ELISA Substrate Solution	Thermo Fisher	PI-34028
human Fc standard	Thermo Fisher	10702-HNAH-5
Expi293™ Expression Medium	Thermo Fisher	A1435103